Static, dynamic and buckling analyses of 3D FGM plates and shells via an isogeometric-meshfree coupling approach

Pengfei Tan[a], Nhon Nguyen-Thanh[a, *], Timon Rabczuk[b], Kun Zhou[a, *]

[a] School of Mechanical and Aerospace Engineering, Nanyang Technological University, 50 Nanyang Avenue, Singapore 639798, Singapore

[b] Institute of Structural Mechanics, Bauhaus-University Weimar, Marienstr. 15, D-99423 Weimar, Germany

Abstract

This paper develops a three-dimensional (3D) isogeometric analysis (IGA) and meshfree coupling approach to investigate the static, dynamic and buckling behaviors for plates and shells of functionally graded material (FGM). The meshfree method and IGA are coupled using the higher-order consistency condition in the physical domain so that the higher-order continuity of basis functions is guaranteed, and the topological complexity of the global volumetric parameterization for IGA to build the 3D geometry can be overcome. By employing IGA elements on the domain boundary and meshfree nodes in the interior domain, the approach preserves the advantages of the exact geometry and flexible discretization in the problem domain. Based on the coupling approach, the analyses for FGM plates and shells are carried out, and the effects of the material volume fraction, the side-to-thickness ratio and the curvature of the cylindrical shell on the deflection, natural frequency, and buckling load are investigated. The coupling approach is verified by comparing with the solutions obtained from other existing theories.

***Keywords*:** Functionally graded material; isogeometric analysis; meshfree method; NURBS; RKPM; coupling approach.

*Corresponding authors: Tel.: +65 6790 5499; fax: +65 6792 4062

kzhou@ntu.edu.sg (K. Zhou)

thanhnhon@ntu.edu.sg (N. Nguyen-Thanh)

1. Introduction

Functionally graded material (FGM) is a type of composite material which possesses smoothly and continuously variable material properties in the thickness direction. The novel combination of material ingredients endows FGM with excellent mechanical performance characteristics such as high strength-to-weight ratio, thermal and corrosion resistance, and fatigue strength. Among FGM structures, plates and shells occupy primary roles in engineering applications such as automobiles, aircrafts, nuclear power plants and medical apparatus.

As FGM plates and shells are increasingly applied to industrial fields, various plate and shell theories have been proposed for the structural analyses. Based on hypotheses for the shear deformation distribution, the 3D geometry can be simplified as a two-dimensional (2D) model for analysis. The 2D theory can be classified into three categories: the classic theory [1], first-order shear deformation theory (FSDT) [2, 3] and higher-order shear deformation theory (HSDT) [4-8]. The classical theory that follows Kirchhoff-Love assumptions is only suitable for thin plates and shells as it neglects the effects of the shear deformation. The FSDT considers the linearly distributed transverse shear deformation, while it may lead to the shear locking and non-zero shear stress boundary condition. The HSDT circumvents the disadvantages of FSDT and obtains more accurate solutions by incorporating high-order terms to approximate the displacement field. Compared with the 2D theories, the 3D analysis models do not involve simplifications and assumptions that may give rise to inaccurate solutions [9]. The 3D theories not only achieve more reliable solutions but also enable clearer physical insights [10]. Furthermore, the 3D models can provide a full frequency spectrum for the dynamic analysis of FGM structures [11, 12]. The 3D static, dynamic and buckling analyses for FGM structures have been conducted by numerous researchers [13-16].

To solve the 2D or 3D analysis formulations for FGM plates and shells, a variety of computational methods have been developed, including analytical solutions and numerical methods such as the finite element method (FEM), meshfree method and isogeometric analysis (IGA). The analytical solutions for the static and dynamic analyses of FGM plates and shells can be found in [12, 15, 17-19]. The conventional FEM is a powerful tool for the FGM structural analyses [20-24]. However, FEM still suffers from limitations such as mesh distortion at large deformations, intensive remeshing requirements [25] and only C^0 continuity between elements, which can be partially overcome by the meshfree method and IGA.

The meshfree method employs a set of arbitrarily scattered nodes to discretize the problem domain without connected elements. Compared with FEM, the meshfree method can obtain a more accurate approximation for complex structures, higher-continuity basis functions, and flexible local refinement. Among a variety of meshfree methods [26-29], the reproducing kernel particle method (RKPM) [30] is one of representative meshfree methods and has been utilized to solve solid mechanics problems [31, 32]. The applications of meshfree methods for the analyses of plates and shells are reported in [33-38]. Additionally, since the Kronecker delta condition is not satisfied in the meshfree method which results in the difficulty to apply the essential boundary condition, several improved meshfree methods have been proposed and employed in the plate analyses [39-45].

IGA proposed by Hughes et al. [46], integrating computer aided design and FEM, has attracted great attentions because of the exact geometry representation, higher-order continuity, flexible *k*-refinement, and robustness for the large deformation. IGA has been extensively applied for structural analyses [47-51], fracture mechanics [52-54] and fluid mechanics [55]. IGA maintains the exact geometry by using the non-uniform rational B-spline (NURBS) as basis functions to create the geometric model, which is a great advantage

for analysing shells and complex structures [56, 57]. In addition, the arbitrary continuity order of NURBS basis functions can be controlled, which is needed for the HSDT [58-61].

To exploit the advantages of the meshfree method and IGA, the coupling of the two methods has been developed recently. Wang *et al*. [62] proposed a coupling of the B-spline basis functions and meshfree shape functions using the reproducing conditions. Since it is defined in the parametric domain, the global geometry parameterization is required. Rosolen *et al*. [63] combined the local maximum entropy meshfree method and IGA in the physical domain, which concisely addresses the volume discretization and flexible local refinement simply. However, the coupling approach only satisfies first-order continuity. Considering the challenges in the two approaches, Valizadeh *et al*. [64] developed an IGA-meshfree coupling approach using higher-order consistency conditions in the physical domain, which preserves the arbitrary approximation order of the coupling basis functions and avoids the complexity of a global parameterization to build the 3D problem domain. Therefore, in this work, the IGA-meshfree coupling approach is used to develop 3D analysis formulations for FGM plates and shells.

In this paper, a novel 3D IGA-meshfree coupling approach is developed to analyze FGM plates and shells. IGA is implemented for the exact description of the geometric model on the domain boundary, while the interior domain is discretized by meshfree nodes. This coupling approach based on the higher-order consistency conditions is established in the physical domain, which has higher-continuity basis functions and alleviates the difficulty to construct 3D complex geometry in the global parametric domain for IGA [64]. The effects of material ingredients, boundary conditions, the plate thickness and the curvature of the cylindrical shell on the deflection, natural frequency and buckling load are investigated. Numerical examples are presented to demonstrate the efficiency and accuracy of the coupling approach.

This paper is outlined as follows. The following section introduces the coupling of the meshfree method and IGA. In Section three, 3D formulations for FGM plates and shells analyses using the IGA-meshfree coupling approach are presented. Several numerical examples for FGM plates and shells are given in Section four. Finally, conclusions are drawn in Section five.

2. IGA-meshfree coupling approach

The basis functions for the NURBS-based IGA and RKPM are provided in this section. The IGA and RKPM are coupled in a narrow boundary region using the consistency conditions.

2.1. NURBS basis functions

NURBS basis functions are built on B-spline basis functions by the projective transformation. In the parametric coordinate, B-spline basis functions are expressed by a non-decreasing set of knot values called knot vector $\Xi = \{\xi_1, \xi_2, \ldots, \xi_{n+p+1}\}$ ($\xi_i \in \mathbb{R}$), where p is the polynomial order and n is the number of basis functions. Starting from the order $p = 0$, the recursive form of the B-spline basis functions is defined as [46]:

$$N_{i,0} = \begin{cases} 1 & \text{if } \xi_i \le \xi \le \xi_{i+1} \\ 0 & \text{otherwise} \end{cases}, \quad \text{for } p = 0, \tag{1}$$

$$N_{i,p}(\xi) = \frac{\xi - \xi_i}{\xi_{i+p} - \xi_i} N_{i,p-1}(\xi) + \frac{\xi_{i+p+1} - \xi}{\xi_{i+p+1} - \xi_{i+1}} N_{i+1,p-1}(\xi), \quad \text{for } p > 0. \tag{2}$$

As three sets of knot vectors $\Xi = \{\xi_1, \xi_2, \ldots, \xi_{n+p+1}\}$, $\mathrm{H} = \{\eta_1, \eta_2, \ldots, \eta_{m+q+1}\}$ and $\Pi = \{\zeta_1, \zeta_2, \ldots, \zeta_{n+p+1}\}$ are given in the ξ, η and ζ directions, respectively, 3D NURBS basis functions are obtained by using the tensor product:

$$R_{i,j,k}(\xi,\eta,\zeta)=\frac{N_{i,p}(\xi)M_{j,q}(\eta)L_{k,r}(\zeta)w_{i,j,k}}{\sum_{\hat{k}=1}^{l}\sum_{\hat{j}=1}^{n}\sum_{\hat{i}=1}^{m}N_{\hat{i},p}(\xi)M_{\hat{j},q}(\eta)L_{\hat{k},r}(\zeta)w_{\hat{i},\hat{j},\hat{k}}}, \tag{3}$$

where $w_{i,j,k}$ is the weight, and $N_{i,p}$, $M_{i,q}$ and $L_{k,r}$ are the basis functions. The NURBS solid is expressed as

$$V(\xi,\eta,\zeta)=\sum_{\hat{k}=1}^{l}\sum_{\hat{j}=1}^{n}\sum_{\hat{i}=1}^{m}R_{i,j,k}(\xi,\eta,\zeta)P_{i,j,k}\ . \tag{4}$$

where m, n and l are the numbers of basis functions in the ξ, η and ζ directions, respectively, and $P_{i,j,k}$ is the control point.

2.2. RKPM basis functions

In the physical problem domain discretized by a set of particles $\{\mathbf{x}_i\}_{i=1}^{N_\mathrm{P}}$, where N_P is the number of meshfree particles, the RKPM basis functions [31] are defined as

$$\psi_i(\mathbf{x})=C(\mathbf{x},\mathbf{x}-\mathbf{x}_i)\phi_a(\mathbf{x}-\mathbf{x}_i), \tag{5}$$

where ϕ_a is the kernel function [65]:

$$\phi_a(s)=\begin{cases}1-6s^2+8s^3-3s^4 & \text{for } s\le 1\\ 0 & \text{for } s>1\end{cases},\ s=\frac{\|\mathbf{x}-\mathbf{x}_i\|}{r_0}, \tag{6}$$

where r_0 is the radius of spherical support domain for the 3D geometry, which is calculated as follows:

$$r_0=\lambda d\ ,\ d=\max\left(|x-x_i|,|y-y_i|,|z-z_i|\right) \tag{7}$$

where λ is the scaling factor taken as 2.5 and d is the maximum distance of adjacent nodes in three axial directions.

The correction function $C(\mathbf{x},\ \mathbf{x}\text{-}\mathbf{x}_i)$ is expressed as a linear combination of polynomial basis functions:

$$C(\mathbf{x},\mathbf{x}-\mathbf{x}_i)=\mathbf{H}^{\mathrm{T}}(\mathbf{x}-\mathbf{x}_i)\mathbf{b}(\mathbf{x}), \tag{8}$$

where the quadratic polynomial is used in this work:

$$\begin{aligned}\mathbf{H}(\mathbf{x}-\mathbf{x}_i) = [1 \;\; (x-x_i) \;\; (y-y_i) \;\; (z-z_i) \;\; (x-x_i)(y-y_i) \\ (y-y_i)(z-z_i) \;\; (z-z_i)(x-x_i) \;\; (x-x_i)^2 \;\; (y-y_i)^2 \;\; (z-z_i)^2]^{\mathrm{T}}\end{aligned}, \tag{9}$$

and the unknown coefficient $\mathbf{b}(\mathbf{x})$ is determined by imposing the p^{th} order reproducing conditions as follows:

$$\sum_{i=1}^{N_{\mathrm{P}}} \psi_{\mathrm{i}}(\mathbf{x})\mathbf{H}(\mathbf{x}-\mathbf{x}_i) = \mathbf{H}(0)\,. \tag{10}$$

The substitution of Eq. (5) into Eq. (10) results in:

$$\mathbf{M}(\mathbf{x})\mathbf{b}(\mathbf{x}) = \mathbf{H}(0)\,, \tag{11}$$

where the moment matrix $\mathbf{M}(\mathbf{x})$ are given as

$$\mathbf{M}(\mathbf{x}) = \sum_{i=1}^{N_{\mathrm{P}}} \mathbf{H}^{\mathrm{T}}(\mathbf{x}-\mathbf{x}_i)\phi_a(\mathbf{x}-\mathbf{x}_i)\mathbf{H}(\mathbf{x}-\mathbf{x}_i)\,. \tag{12}$$

Hence, $\mathbf{b}(\mathbf{x})$ is expressed as

$$\mathbf{b}(\mathbf{x}) = \mathbf{M}^{-1}(\mathbf{x})\mathbf{H}(0)\,. \tag{13}$$

Substituting Eq. (13) into Eq. (5), the RKPM basis functions can be obtained as

$$\psi_i(\mathbf{x}) = \mathbf{H}^{\mathrm{T}}(0)\mathbf{M}^{-1}(\mathbf{x})\mathbf{H}(\mathbf{x}-\mathbf{x}_i)\phi_a(\mathbf{x}-\mathbf{x}_i)\,. \tag{14}$$

2.3. IGA-RKPM coupling basis functions

The NURBS basis functions for IGA are defined in the parametric domain, while RKPM basis functions are given in the physical domain. In order to establish the coupling basis functions in the physical domain without the global geometry parameterization, NURBS basis functions in the parametric domain need to be mapped into the physical domain. To achieve this aim, the coupling domain is first defined using the volume patch parameterization of IGA in Eq. (4). Since only a single layer of elements is needed on the domain boundary, one domain layer is rewritten as

$$V(\xi,\eta,\zeta)=\sum_{k=1}^{r+1}\sum_{j=1}^{n}\sum_{i=1}^{m}R_{i,j,k}(\xi,\eta,\zeta)P_{i,j,k}\,, \tag{15}$$

where r is the polynomial order in the ζ direction. As a point $\mathbf{x}$ in the physical domain is given, the corresponding coordinate in the parametric space can be obtained:

$$[\xi,\eta,\zeta]=V^{-1}(\mathbf{x})\,. \tag{16}$$

Hence, the NURBS basis function can be expressed in the physical domain:

$$\overset{\circ}{R}_{i,j,k}(\mathbf{x})=R_{i,j,k}(V^{-1}(\mathbf{x}))\,. \tag{17}$$

In the coupling domain, the displacement is represented by a mixed approximation as follows [64]:

$$\begin{aligned}\mathbf{u}(\mathbf{x})&=\mathbf{u}^{\mathrm{IGA}}(\mathbf{x})+\mathbf{u}^{\mathrm{RKPM}}(\mathbf{x})\\&=\sum_{i=1}^{N_{\mathrm{I}}}\overset{\circ}{R}_i(\mathbf{x})u_i+\sum_{j=1}^{N_{\mathrm{R}}}\overline{\psi}_j(\mathbf{x})u_j\end{aligned}\,, \tag{18}$$

where N_{I} and N_{R} are the numbers of NURBS and RKPM basis functions, respectively. By imposing the p^{th} order consistency condition on the mixed displacement approximation in Eq. (18), the following equation can be obtained:

$$\sum_{i=1}^{N_{\mathrm{I}}}\overset{\circ}{R}_i(\mathbf{x})\mathbf{H}(\mathbf{x}-\mathbf{x}_i)+\sum_{j=1}^{N_{\mathrm{R}}}\overline{\psi}_j(\mathbf{x})\mathbf{H}(\mathbf{x}-\mathbf{x}_j)=\mathbf{H}(0)\,. \tag{19}$$

By substituting RKPM basis function in Eq. (8), Eq. (21) can be rewritten as

$$\sum_{i=1}^{N_{\mathrm{R}}}\mathbf{H}^{\mathrm{T}}(\mathbf{x}-\mathbf{x}_i)\mathbf{b}(\mathbf{x})\phi_a(\mathbf{x}-\mathbf{x}_i)\mathbf{H}(\mathbf{x}-\mathbf{x}_i)=\mathbf{H}(0)-\sum_{j=1}^{N_{\mathrm{I}}}\overset{\circ}{R}_j(\mathbf{x})\mathbf{H}(\mathbf{x}-\mathbf{x}_j)\,. \tag{20}$$

After rearranging the terms, the following formula can be obtained:

$$\mathbf{b}(\mathbf{x})=\mathbf{M}^{-1}(\mathbf{x})(\mathbf{H}(0)-\mathbf{a}(\mathbf{x}))\,, \tag{21}$$

where

$$\mathbf{M}(\mathbf{x})=\sum_{i=1}^{N_{\mathrm{R}}}\mathbf{H}^{\mathrm{T}}(\mathbf{x}-\mathbf{x}_i)\phi_a(\mathbf{x}-\mathbf{x}_i)\mathbf{H}(\mathbf{x}-\mathbf{x}_i)\,, \tag{22}$$

$$\mathbf{a}(\mathbf{x}) = \sum_{j=1}^{N_{\mathrm{I}}} \hat{R}_j(\mathbf{x})\mathbf{H}(\mathbf{x}-\mathbf{x}_j)\,. \tag{23}$$

Then substituting the **b**(**x**) in Eq. (21) into Eq. (5), the basis functions in the coupling domain are given as

$$\bar{\psi}_j(\mathbf{x}) = \mathbf{H}^{\mathrm{T}}(\mathbf{x}-\mathbf{x}_j)\mathbf{M}^{-1}(\mathbf{x})(\mathbf{H}(0)-\mathbf{a}(\mathbf{x}))\phi_a(\mathbf{x}-\mathbf{x}_j)\,. \tag{24}$$

One-dimensional (1D) and 2D basis functions with the meshfree domain (Ω^{MF}) and coupling domain (Ω^{CP}) for the IGA-meshfree coupling approach are illustrated in Figs. 1 and 2, respectively. The continuity of the coupling basis functions can be examined by calculating the consistency conditions. Errors of the second-order consistency conditions given in Eq. 19 for 1D basis function are provided in Fig. 3. e_1 and e_2 represent the errors of the first-order and second-order consistency:

$$e_1 = \sum_{i=1}^{N_{\mathrm{I}}} \hat{R}_i(\mathbf{x})(x-x_i) + \sum_{j=1}^{N_{\mathrm{R}}} \bar{\psi}_j(\mathbf{x})(x-x_i)\,, \tag{25}$$

$$e_2 = \sum_{i=1}^{N_{\mathrm{I}}} \hat{R}_i(\mathbf{x})(x-x_i)^2 + \sum_{j=1}^{N_{\mathrm{R}}} \bar{\psi}_j(\mathbf{x})(x-x_i)^2\,. \tag{26}$$

The errors are very small (around 10^{-17}), which means that the second-order consistency conditions are satisfied by the coupling basis functions.

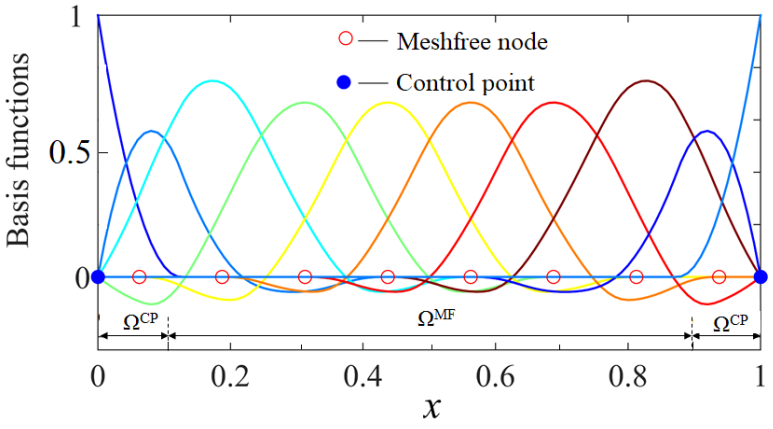

Fig. 1. Basis functions of the IGA-meshfree coupling approach with p = 2 in 1D.

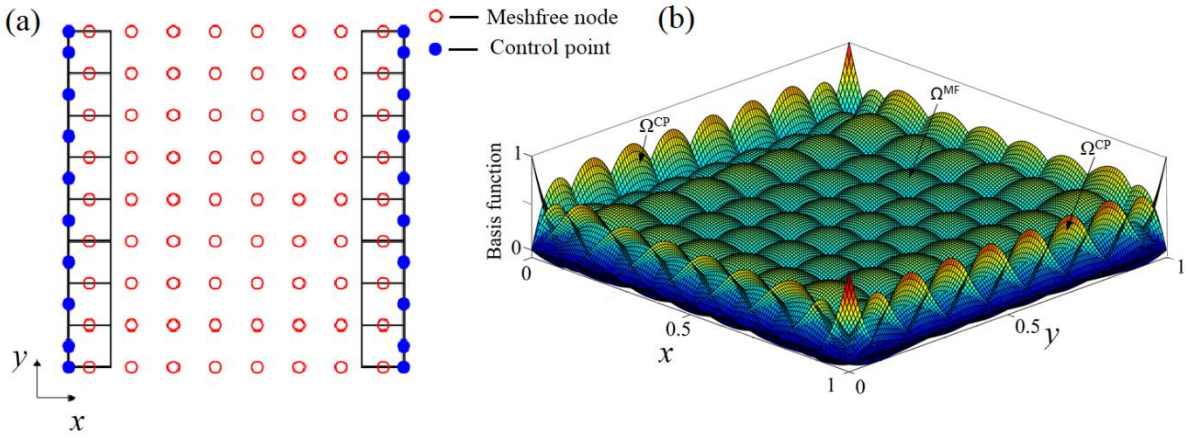

Fig. 2. (a) Distribution of meshfree nodes and control points and (b) basis functions of the IGA-meshfree coupling approach with $p = 2$ in 2D.

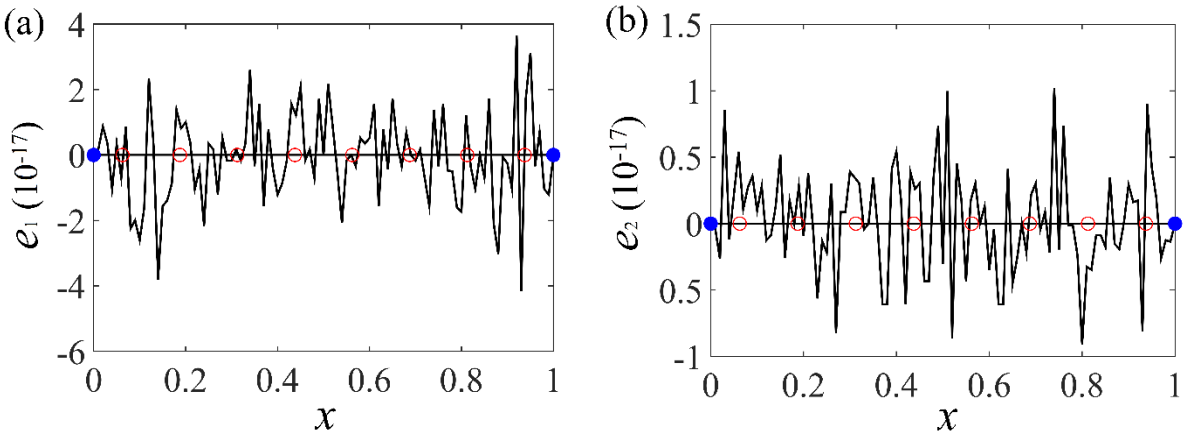

Fig. 3. Errors of (1) first-order and (b) second-order consistency condition equations.

3. D formulations for FGM plates and shells analyses

3.1. Functionally graded material

FGM belongs to the class of composite materials that has a smooth and continuous distribution of material properties, with an example of a rectangular FGM plate shown in Fig. 4. In this work, two techniques which include the rule of mixture law and exponential

variation method are used to describe the material properties distribution for the FGM plates and shells. The volume fractions of two materials are estimated by the power-law function:

$$V_{\mathrm{t}}(z)=\left(\frac{1}{2}+\frac{z}{h}\right)^{n},\ \ V_{\mathrm{b}}(z)=1-V_{\mathrm{t}}(z), \tag{27}$$

where V_{t} and V_{b} denote the volume fractions of the top and bottom materials, respectively; h is the thickness; the power index n determines the material constituent contents. According to the rule of mixture law, when two material compositions are ceramic at the top and metal at the bottom, respectively, the material properties are defined as

$$M\left(z\right)=M_{\mathrm{c}}V_{\mathrm{t}}\left(z\right)+V_{\mathrm{b}}\left(z\right)M_{\mathrm{m}}, \tag{28}$$

where subscripts c and m denote the ceramic and metal, respectively; M(z) represents FGM properties at z = 0, including the Young's modulus E(z), the Poisson ratio v(z) and the mass density ρ(z). From Eqs. (27) and (28), the distributions of the Young's modulus in the thickness direction for the Al/Al_2O_3 plate with different power indices n are plotted in Fig. 5. The second technique that approximates the material properties variation with the exponential function in the thickness direction has been adopted in [15, 66, 67]:

$$M(z)=M_{\mathrm{c}}\exp(n(\frac{1}{2}+\frac{z}{h})). \tag{29}$$

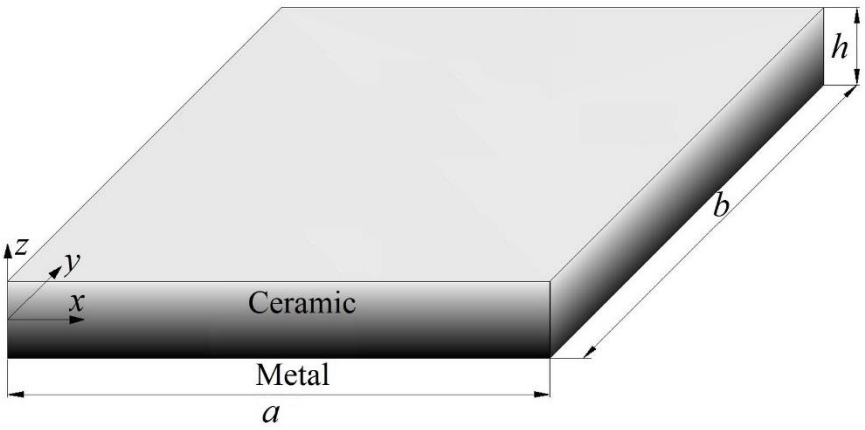

Fig. 4. Geometric model for the rectangular FGM plate.

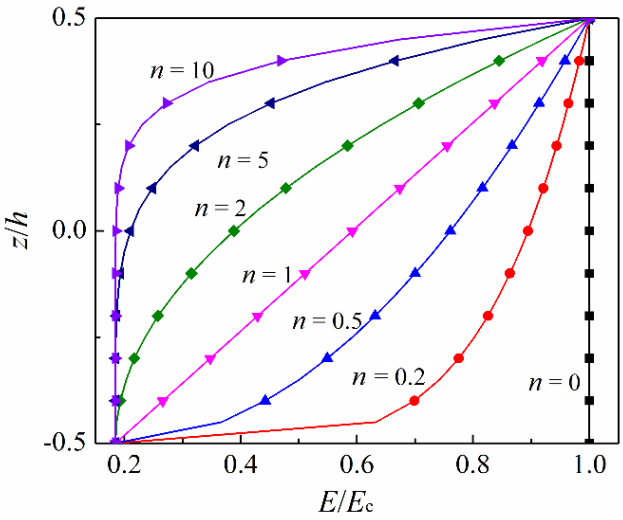

Fig. 5. Distributions of the Young's modulus in the thickness direction for the Al/Al_2O_3 plate with different power indices *n*.

3.2. Constitutive formulations for static, dynamic and buckling analyses

Considering a problem domain Ω with a boundary Γ, the dynamic equilibrium of the strain energy, work done and kinetic energy is expressed as [59]

$$\int_\Omega \delta\boldsymbol{\varepsilon}^{\mathrm{T}}\boldsymbol{\sigma}\mathrm{d}\Omega - \int_\Omega \delta\mathbf{u}^{\mathrm{T}}\rho\ddot{\mathbf{u}}\mathrm{d}\Omega = \int_\Gamma \delta\mathbf{u}^{\mathrm{T}}\mathbf{t}\mathrm{d}\Gamma + \int_\Omega \delta\mathbf{u}^{\mathrm{T}}\mathbf{b}\mathrm{d}\Omega\,, \tag{30}$$

where $\boldsymbol{\varepsilon}$ is the strain, $\boldsymbol{\sigma}$ is the stress, $\mathbf{b}$ is the body force, $\mathbf{t}$ is the traction on the natural boundary, ρ is the density, $\mathbf{u}$ is the displacement, and $\ddot{\mathbf{u}}$ is the acceleration.

Based on the principle of virtual work, the weak form for the static analysis for the plate under the transverse loading q_0 on the top surface is expressed as

$$\int_\Omega \delta\boldsymbol{\varepsilon}^{\mathrm{T}}\boldsymbol{\sigma}\mathrm{d}\Omega = \int_\Gamma \delta w q_0 \mathrm{d}\Gamma\,. \tag{31}$$

For the free vibration analysis of the plate, a weak form can be derived from Eq. (30):

$$\int_\Omega \delta\boldsymbol{\varepsilon}^{\mathrm{T}}\boldsymbol{\sigma}\mathrm{d}\Omega = \int_\Omega \delta\mathbf{u}^{\mathrm{T}}\rho\ddot{\mathbf{u}}\mathrm{d}\Omega\,. \tag{32}$$

In the case of the pre-buckling analyses under the in-plane forces, the weak form is given as [68]

$$\int_\Omega \delta\boldsymbol{\varepsilon}^{\mathrm{T}}\boldsymbol{\sigma}\mathrm{d}\Omega = \int_\Omega (\nabla\delta\mathbf{u})^{\mathrm{T}}\mathbf{N}_0\nabla\mathbf{u}\mathrm{d}\Omega, \tag{33}$$

where

$$\nabla = \begin{bmatrix} \frac{\partial}{\partial x} & \frac{\partial}{\partial y} & \frac{\partial}{\partial z} & 0 & 0 & 0 & 0 & 0 & 0 \\ 0 & 0 & 0 & \frac{\partial}{\partial x} & \frac{\partial}{\partial y} & \frac{\partial}{\partial z} & 0 & 0 & 0 \\ 0 & 0 & 0 & 0 & 0 & 0 & \frac{\partial}{\partial x} & \frac{\partial}{\partial y} & \frac{\partial}{\partial z} \end{bmatrix}^{\mathrm{T}}, \ \mathbf{N}_0 = \begin{bmatrix} \mathbf{S}_{\mathrm{g}} & 0 & 0 \\ 0 & \mathbf{S}_{\mathrm{g}} & 0 \\ 0 & 0 & \mathbf{S}_{\mathrm{g}} \end{bmatrix}, \ \mathbf{S}_{\mathrm{g}} = \begin{bmatrix} \sigma_{xx}^0 & \sigma_{xy}^0 & \sigma_{zx}^0 \\ \sigma_{xy}^0 & \sigma_{yy}^0 & \sigma_{yz}^0 \\ \sigma_{zx}^0 & \sigma_{yz}^0 & \sigma_{zz}^0 \end{bmatrix}, \tag{34}$$

where σ_{ij}^0 ($i, j = x, y,$ or z) are the pre-buckling stresses generated from the load.

The strain $\boldsymbol{\varepsilon}$ and stress $\boldsymbol{\sigma}$ are, respectively, written as

$$\boldsymbol{\varepsilon} = \mathbf{L}\mathbf{u}, \ \boldsymbol{\sigma} = \mathbf{D}\boldsymbol{\varepsilon}, \tag{35}$$

where

$$\mathbf{L} = \begin{bmatrix} \frac{\partial}{\partial x} & 0 & 0 & \frac{\partial}{\partial y} & 0 & \frac{\partial}{\partial z} \\ 0 & \frac{\partial}{\partial y} & 0 & \frac{\partial}{\partial x} & \frac{\partial}{\partial z} & 0 \\ 0 & 0 & \frac{\partial}{\partial z} & 0 & \frac{\partial}{\partial y} & \frac{\partial}{\partial x} \end{bmatrix}^{\mathrm{T}}, \ \mathbf{D} = \frac{E(z)(1-\nu(z))}{(1+\nu(z))(1-2\nu(z))} \begin{bmatrix} D_{11} & D_{12} & D_{12} & 0 & 0 & 0 \\ D_{12} & D_{11} & D_{12} & 0 & 0 & 0 \\ D_{12} & D_{12} & D_{11} & 0 & 0 & 0 \\ 0 & 0 & 0 & D_{22} & 0 & 0 \\ 0 & 0 & 0 & 0 & D_{22} & 0 \\ 0 & 0 & 0 & 0 & 0 & D_{22} \end{bmatrix}, \tag{36}$$

where $E(z)$ is the Young's modulus, $\nu(z)$ is the Poisson ratio, and

$$D_{11} = 1, D_{12} = \frac{\nu(z)}{1-\nu(z)}, D_{22} = \frac{(1-2\nu(z))}{2(1-\nu(z))}. \tag{37}$$

The displacement field of 3D plates or shells can be approximated as

$$\mathbf{u} = \sum_A^n \hat{R}_A\mathbf{u}_A, \ \hat{R}_A = \begin{cases} \bar{\psi}_A(\mathbf{x}), & \text{for coupling domain} \\ \psi_A(\mathbf{x}), & \text{for meshfree domain} \end{cases}, \tag{38}$$

where $\hat{R}_A$ can be either RKPM basis functions in the meshfree domain or IGA-meshfree basis functions in the coupling domain, and $\mathbf{u}_A = [u_A \ v_A \ w_A]^{\mathrm{T}}$ is the displacement vector. Substituting Eq. (38) into Eq. (35), the strains are expressed as

$$\boldsymbol{\varepsilon}=\sum_{A=1}^{n}\mathbf{B}_A\mathbf{u}_A\ ,\ \mathbf{B}_A=\begin{bmatrix} R_{A,x} & 0 & 0 & R_{A,y} & 0 & R_{A,z} \\ 0 & R_{A,y} & 0 & R_{A,x} & R_{A,z} & 0 \\ 0 & 0 & R_{A,z} & 0 & R_{A,y} & R_{A,x} \end{bmatrix}^{\mathrm{T}}. \tag{39}$$

According to Eqs. (35) and (39), the formulations for static analysis can be rewritten in the following matrix form:

$$\mathbf{K}\mathbf{u}=\mathbf{f}\ , \tag{40}$$

where **K** and **f** are the global stiffness matrix and the force vector

$$\mathbf{K}=\int_{\Omega}\mathbf{B}_A^{\mathrm{T}}\mathbf{D}\mathbf{B}_A\mathrm{d}\Omega\ ,\mathbf{f}=\int_{\Gamma}q_0\mathbf{R}_A\mathrm{d}\Gamma\ ,\ \mathbf{R}_A=\begin{bmatrix}0 & 0 & R_A\end{bmatrix}. \tag{41}$$

Substituting Eqs. (35) and (39) into Eq. (32), the matrix form of the consistent dynamic analysis can be rewritten by

$$(\mathbf{K}-\omega^2\mathbf{M})\mathbf{u}=0\ , \tag{42}$$

where ω is the natural frequency, and **M** is the global mass matrix expressed as

$$\mathbf{M}=\int_{\Omega}\mathbf{N}_A^{\mathrm{T}}\rho(z)\mathbf{N}_A d\Omega\ ,\ \mathbf{N}_A=\begin{bmatrix} R_A & 0 & 0 \\ 0 & R_A & 0 \\ 0 & 0 & R_A \end{bmatrix}. \tag{43}$$

Based on the weak form for the buckling in Eq. (33), the buckling analysis formulation is given in the matrix form:

$$(\mathbf{K}+\lambda_{\mathrm{cr}}\mathbf{K}_{\mathrm{g}})\mathbf{u}=0\ , \tag{44}$$

where λ_{cr} is the critical buckling value, and the geometric stiffness matrix $\mathbf{K}_{\mathrm{g}}$ is expressed as

$$\mathbf{K}_{\mathrm{g}}=\int_{\Omega}\mathbf{G}_A^{\mathrm{T}}\mathbf{N}_0\mathbf{G}_A d\Omega\ , \tag{45}$$

where

$$\mathbf{G}_A=\begin{bmatrix} R_{A,x} & R_{A,y} & R_{A,z} & 0 & 0 & 0 & 0 & 0 & 0 \\ 0 & 0 & 0 & R_{A,x} & R_{A,y} & R_{A,z} & 0 & 0 & 0 \\ 0 & 0 & 0 & 0 & 0 & 0 & R_{A,x} & R_{A,y} & R_{A,z} \end{bmatrix}^{\mathrm{T}}. \tag{46}$$

4. Numerical examples

In the section, the static, dynamic and buckling analyses is conducted using the 3D IGA-meshfree coupling approach for FGM plates and shells. The coupling approach is validated by comparing with previous reference solutions.

4.1. Static analysis for FGM plates

Two examples for static analyses of FGM plates are presented, including rectangular as shown in Fig. 4 and circular plates as shown in Fig. 10. The materials for FGM ingredients used in this work are listed in Table 1. Two boundary conditions are employed: the simply supported (S) boundary condition:

$$\begin{aligned} v = w = 0, \quad & \text{at } x = 0,\ a \\ u = w = 0, \quad & \text{at } y = 0,\ b \end{aligned}, \tag{47}$$

and the clamped (C) boundary condition:

$$u = v = w = 0, \quad \text{at } x = 0,\ a \text{ and } y = 0,\ b\,. \tag{48}$$

The essential boundary conditions are weakly enforced using the Nitsche's method [64, 69].

Table 1. Materials properties for the FGM.

Properties	**Al**	**Ti**	**ZrO_2-1**	**ZrO_2-2**	**ZrO_2-3**	**Al_2O_3**
E (GPa)	70	110.25	278.41	200	151	380
v	0.3	0.288	0.288	0.3	0.3	0.3
ρ (kg/m^3)	2707	-	-	5700	3000	3800

4.1.1. Rectangular plate

A rectangular FGM plate as shown in Fig. 4 is subjected to the sinusoidal or uniform load on the top surface. The normalized central deflection for the Al/Al_2O_3 plate via degrees of freedom (DOFs) with a/h = 10 and 20 is investigated in Fig. 7. In the z direction, two layers of control points are on the top and bottom surfaces, respectively, and 3 meshfree

nodes are filled inside the interior domain. We can see that the present approach with 3561 DOFs (15 × 15 × 3 meshfree nodes and 16 × 16 × 2 control points) can achieve accurate solution comparing with the existing results.

The meshes of the FGM plate in the *x*-*y* and *x*-*z* planes are demonstrated in Figs. 6 (a) and (b), respectively. The top and bottom surfaces are discretized using IGA elements. In the *z* direction, one element with 3 control points (second polynomial order) is implemented, while only control points defining the surface boundary have degrees of freedom for the analysis as displayed in Fig. 6 (b). IGA elements form the IGA-meshfree coupling domain. The meshfree nodes are located inside the domain between two surfaces.

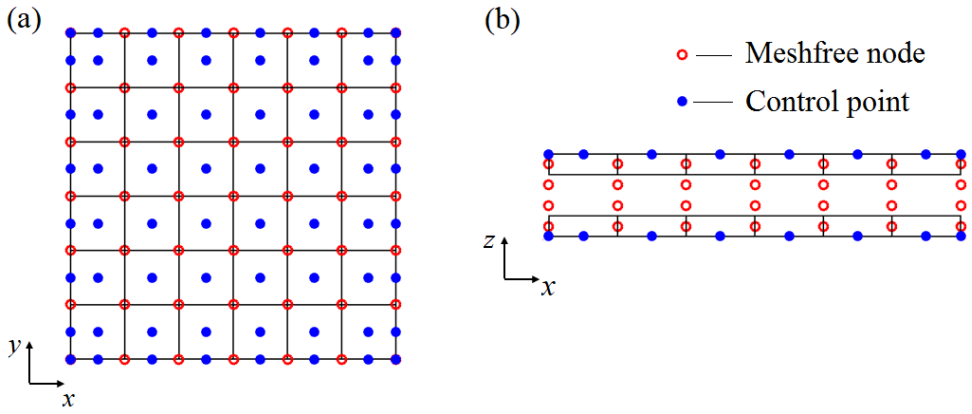

Fig. 6. Distribution of control points and meshfree nodes for the FGM plate: (a) *x*-*y* and (b) *x*-*z* planes.

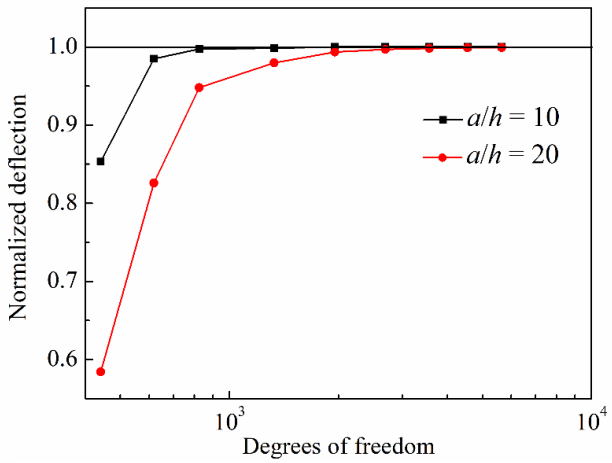

Fig. 7. Convergence test of the normalized central deflection for the Al/Al_2O_3 rectangular plate with $n = 1$ [70].

An Al/Al_2O_3 plate subjected to sinusoidal load $f_0\sin(\pi x/a)\sin(\pi y/b)$ is first investigated. The material properties in the thickness direction are computed by the rule of mixtures of Eqs. (27) and (28). The comparison of the dimensionless central deflection $\overline{W} = 10W(a/2, b/2, 0)E_c h^3/(f_0 a^4)$ for the simply supported Al/Al_2O_3 plate with various ratios a/h and power indices n is summarized in Table 2. The present results are in good agreement with that obtained by other methods [11, 52, 59, 70]. Furthermore, the dimensionless central deflection $\overline{W} = 10W(a/2, b/2, 0)E_m h^3/\{12(1-\nu)f_0 a^4\}$ for an Al/ZrO_2-2 plate under uniform load with SSSS and CCCC boundary conditions are listed in Table 3. Comparing with the SSSS boundary condition, the CCCC boundary condition has more constraints, which results in the increase of structural stiffness. Hence, the deflection of the FGM plate under the CCCC boundary condition is smaller. From the comparison, we can see that the present solutions with different power indices agree well with the existing results from refined plate theory (RPT) [59], HSDT [70] and meshless local Petrov-Galerkin (MLPG) [71]. The deflection shapes of the FGM plate under SSSS, CCCC, SFSF and CFCF boundary conditions are shown in Fig. 8. Here, F denotes the free boundary condition.

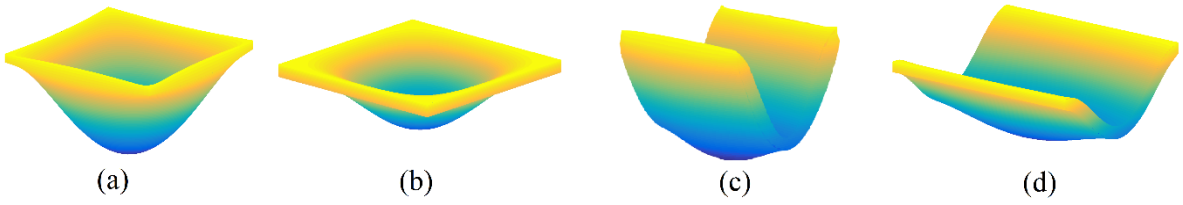

Fig. 8. Deflection of the Al/Al_2O_3 plate with (a) SSSS, (b) CCCC, (c) SFSF and (d) CFCF boundary conditions (a/h = 20, n = 1).

Table 2. Comparison of the dimensionless central deflection for the simply supported Al/Al_2O_3 plate under sinusoidal distributed load.

a/*h*	Method	Power index *n*			
		0.5	**1**	**4**	**10**
4	Present	0.5538	0.7182	1.1622	1.3793
	3D IGA [11]	-	0.7171	1.1585	1.3790
	IGA [52]	0.5654	0.7284	1.1599	1.3908
	HSDT [70]	0.5654	0.7284	1.1599	1.3909
10	Present	0.4518	0.5875	0.8825	1.0077
	3D IGA [11]	-	0.5875	0.8822	1.0083
	IGA [52]	0.4537	0.5889	0.8815	1.0087
	RPT [59]	0.4537	0.5890	0.8816	1.0085
20	Present	0.4368	0.5684	0.8414	0.9532
	IGA [52]	0.4376	0.5689	0.8414	0.9537
	HSDT [70]	0.4377	0.5689	0.8415	0.9538

Table 3. Comparison of the dimensionless central deflection for the Al/ZrO_2-2 plate under uniform load with different boundary conditions (a/h = 5).

Boundary condition	Method	Power index *n*					
		Ceramic	**0.5**	**1**	**2**	**8**	**Metal**
SSSS	Present	0.1686	0.2527	0.2932	0.3314	0.3919	0.4816
	RPT [59]	0.1703	0.2536	0.2934	0.3312	0.3922	0.4865
	HSDT [70]	0.1716	0.2554	0.2955	0.3334	0.3958	0.4903
	MLPG [71]	0.1671	0.2505	0.2905	0.3280	-	0.4775
CCCC	Present	0.0738	0.1083	0.1262	0.1457	0.1770	0.2109
	RPT [59]	0.0701	0.1029	0.1201	0.1384	0.1669	0.2001
	HSDT [70]	0.0734	0.1077	0.1256	0.1447	0.1760	0.2098
	MLPG [71]	0.0731	0.1073	0.1253	0.1444	-	0.2088

4.1.2. Circular plate

In this example, the bending of a circular FGM plate subjected to the uniform load on the top surface as shown in Fig. 10 is analyzed. The nodes distribution of the circular plate is illustrated in Fig. 11. The curved edge around the circular plate is meshed using IGA elements and the interial domain is discretized with meshfree nodes.

To check the convergence performance of the coupling approach compared with the meshfree method, an example for the static analysis of the circular Ti/ZrO_2-1 plate is presented. The circular plate subjected to the sinusoidal load is under clamped boundary conditions. The relative error of the central deflection is given in Fig. 9. The relative error ε_r is calculated by $\varepsilon_r = |(u - u_{ref})/u_{ref}|$, where u is the central deflection and u_{ref} is the reference result obtained by 3D IGA [11]. It can be observed that the coupling approach can converge with less degrees of freedom and get a smaller relative error.

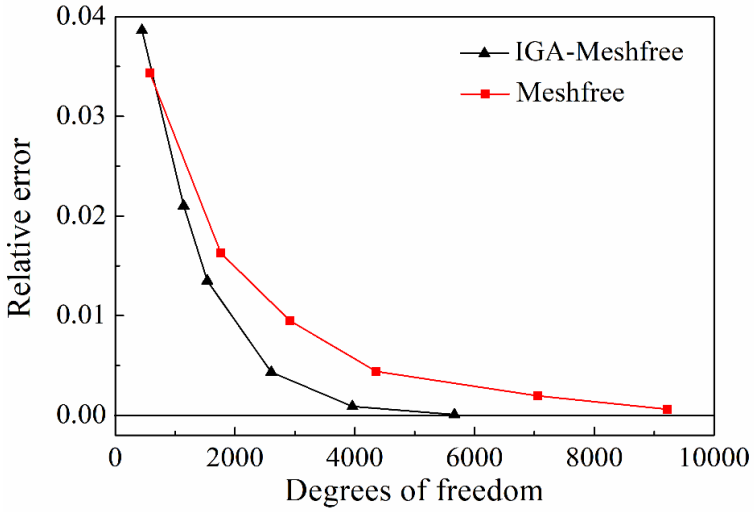

Fig. 9. Relative error of the central deflection for the circular (n = 2, R/h = 10) Ti/ZrO_2-1 plate.

Based on the rule of mixture method, the material properties are described by

$$V_b(z) = \left(\frac{1}{2} - \frac{z}{h}\right)^n, \quad V_t(z) = 1 - V_b(z), \tag{49}$$

$$E(z) = E_m V_b(z) + E_c V_t(z)$$
$$\rho(z) = \rho_m V_b(z) + \rho_c V_t(z) \quad (50)$$

The pure ceramic and metal materials are located at the top and bottom surfaces, respectively. Poisson's ratio is assumed to be a constant taken as 0.3. The central deflection is normalized with $\bar{W} = 64 W_O E_c h^3/\{12(1-\nu^2) f_0 R^4\}$. A Ti/$ZrO_2$-1 plate under uniform load and clamped boundary condition is considered to investigate the bending behavior. The comparison of the central displacement with other solutions obtained by the 3D IGA [11], HSDT [58] and FSDT [72] is conducted in Table 4. It is observed that a good agreement with other results is achieved. Furthermore, the deflection shapes of the Ti/ZrO_2-1circular plate under simply supported and clamped boundary conditions are illustrated in Fig. 12.

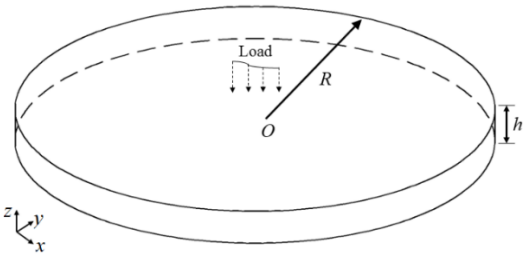

Fig. 10. Circular FGM plate model.

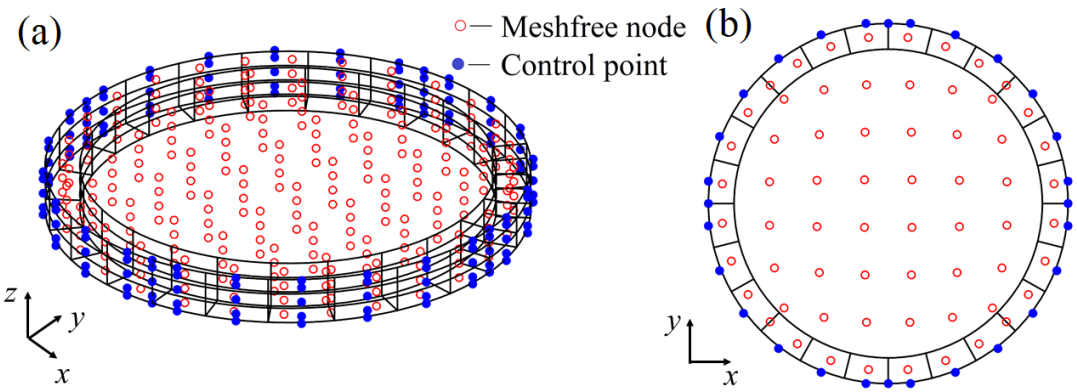

Fig. 11. Distribution of the meshfree nodes and control points for the circular plate: (a) 3D mesh and (b) *x*-*y* plane.

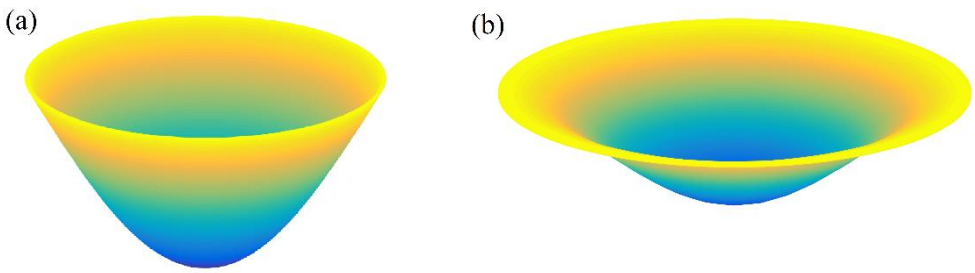

Fig. 12. Deflection of the Ti/ZrO_2-1circular plate under (a) simply supported and (b) clamped boundary conditions (R/h = 100, n = 1).

Table 4. Comparison of the dimensionless central deflection for the Ti/ZrO_2-1 plate under uniform load and clamped boundary condition.

h*/*R	**Method**	**Power index *n***					
		0	**2**	**4**	**8**	**10**	**10^4**
0.05	Present	2.5302	1.3825	1.2633	1.1654	1.1391	0.9982
	3D IGA [11]	2.5353	1.3919	1.2722	1.1725	1.1460	1.0040
	HSDT [58]	2.5480	1.3990	1.2786	1.1785	1.1520	1.0092
	FSDT [72]	2.554	1.402	1.282	1.181	1.155	1.011
0.1	Present	2.6186	1.4316	1.3083	1.2065	1.1778	1.0363
	3D IGA [11]	2.6175	1.4317	1.3079	1.2065	1.1796	1.0365
	HSDT [58]	2.6297	1.4386	1.3143	1.2123	1.1855	1.0415
	FSDT [72]	2.639	1.444	1.320	1.217	1.190	1.045
0.15	Present	2.7562	1.4998	1.3698	1.2642	1.2375	1.0919
	3D IGA [11]	2.7547	1.4982	1.3677	1.2633	1.2359	1.0908
	HSDT [58]	2.7652	1.5043	1.3733	1.2685	1.2412	1.0952
	FSDT [72]	2.781	1.515	1.384	1.278	1.250	1.101
0.2	Present	2.9470	1.5918	1.4519	1.3443	1.3153	1.1669
	3D IGA [11]	2.9463	1.5913	1.4513	1.3427	1.3146	1.1667
	HSDT [58]	2.9541	1.5958	1.4557	1.3467	1.3187	1.1700
	FSDT [72]	2.979	1.613	1.473	1.362	1.333	1.180

The dimensionless central deflection for rectangular Al/Al_2O_3 plate via the side-to-thickness ratio a/h and circular Ti/ZrO_2-1 plate via the radius-to-thickness ratio R/h is

displayed in Fig. 13. The dimensionless deflection decreases sharply with increasing plate thickness when the ratio a/h or R/h is less than 10. As the plate becomes thinner, the change of the dimensionless deflection with the thickness is small. From both the rectangular and circular plates, we find that the larger metallic ingredient results in the increase of the dimensionless deflection because the metal has a smaller stiffness than that of the ceramic.

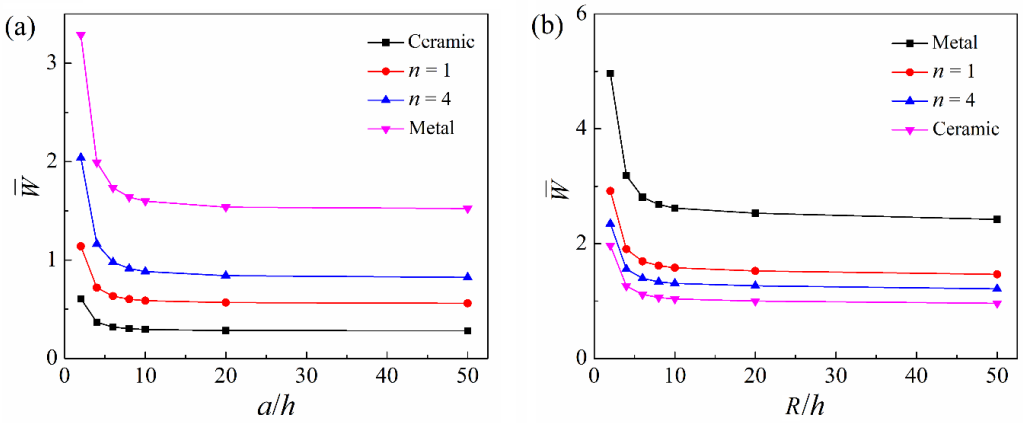

Fig. 13. Dimensionless central deflection for (a) rectangular FGM plate via the ratio a/h and (b) circular FGM plate via the ratio R/h.

4.2. Dynamic analyses of FGM plates and shells

In the section, the dynamic behavior of the FGM plates and shells is analyzed including the rectangular plate, circular plate and cylindrical shell. The effects of the material compositions, side-to-thickness ratio and curvature of the cylindrical shell on the natural frequency are studied.

4.2.1. Rectangular plate

The geometric model of the rectangular FGM plate is shown in Fig. 4. A simply supported Al/Al_2O_3 plate with the material properties given in Table 1 is first considered to investigate the natural frequency. The rule of mixture law in Eqs. (27) and (28) is applied to describe the distribution of material properties. The dimensionless natural frequency is

normalized with $\bar{\omega} = \omega h\sqrt{\rho_c/E_c}$. The convergence test for the Al/Al_2O_3 plate is shown in Fig. 14. We can see that good accuracy can be achieved as 4545 DOFs (17 × 17 × 3 meshfree nodes and 18 × 18 × 2 control points) are applied.

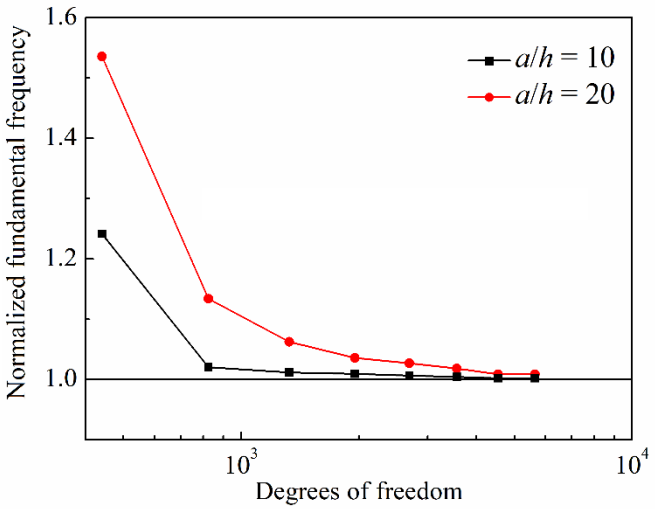

Fig. 14. Convergence test of the normalized fundamental frequency for the simply supported Al/Al_2O_3 plate with $n = 1$ [71].

Table 5. Comparison of the dimensionless fundamental frequency for the simply supported Al/Al_2O_3 plate with various ratios a/h and power indices n.

a/*h*	Method	Power index *n*					
		Ceramic	**0.5**	**1**	**4**	**10**	**Metal**
5	Present	0.2127	0.1822	0.1646	0.1389	0.1312	0.1086
	HSDT [71]	0.2121	0.1819	0.1640	0.1383	0.1306	0.1077
	TSDT [73]	0.2112	0.1805	0.1631	0.1397	0.1324	0.1076
	FSDT [74]	0.2112	0.1806	0.1650	0.1371	0.1304	0.1075
10	Present	0.0581	0.0494	0.0445	0.0384	0.0367	0.0299
	HSDT [71]	0.0577	0.0492	0.0443	0.0381	0.0364	0.0293
	TSDT [73]	0.0577	0.049	0.0442	0.0382	0.0366	0.0293
	FSDT [74]	0.0577	0.0492	0.0445	0.0383	0.0363	0.0294
20	Present	0.0149	0.0127	0.0114	0.0100	0.0095	0.0077
	HSDT [71]	0.0146	0.0124	0.0112	0.0097	0.0093	-
	TSDT [73]	0.0148	0.0125	0.0113	0.0098	0.0094	-
	FSDT [74]	0.0148	0.0128	0.0115	0.0101	0.0096	-

The comparison of the dimensionless fundamental frequency with various ratios a/h and power indices n is presented in Table 5. We can see that the present results agree well with the solutions obtained by HSDT using IGA [71], third-order shear deformation theory (TSDT) [73] and FSDT [74]. The first five dimensionless fundamental frequencies $\bar{\omega} = \omega h\sqrt{\rho_{\mathrm{m}}/E_{\mathrm{m}}}$ for the simply supported Al/ZrO_2-2 plate with various power indices are given in Table 6. The obtained frequency have a good accuracy compared with the solutions calculated by the meshfree method [75] and IGA [71]. Moreover, the first four vibration modes of the FGM plate under SSSS, CCCC and SFSF boundary conditions are demonstrated in Fig. 15.

Table 6. Comparison of the first five dimensionless frequencies for the simply supported Al/ZrO_2-2 FGM plate with various power indices n at a/h = 5.

n	**Method**	**Mode number**				
		1	**2**	**3**	**4**	**5**
Ceramic	Present	0.2477	0.4539	0.4539	0.5431	0.5431
	HSDT [71]	0.2461	0.4539	0.4539	0.5385	0.5385
	Meshfree [75]	0.2457	0.4483	0.4484	0.5395	0.5395
1	Present	0.2200	0.4118	0.4118	0.4831	0.4831
	HSDT [71]	0.2185	0.4118	0.4118	0.4794	0.4794
	Meshfree [75]	0.2188	0.3992	0.3992	0.4779	0.4779
2	Present	0.2204	0.4039	0.4039	0.4803	0.4803
	HSDT [71]	0.2190	0.4039	0.4039	0.4768	0.4768
	Meshfree [75]	0.2188	0.3991	0.3992	0.4779	0.4779
5	Present	0.2232	0.3967	0.3967	0.4826	0.4826
	HSDT [71]	0.2216	0.3967	0.3967	0.4783	0.4783
	Meshfree [75]	0.2215	0.3921	0.3922	0.4794	0.4795
Metal	Present	0.2131	0.3897	0.3897	0.4669	0.4669
	HSDT [71]	0.2113	0.3897	0.3897	0.4623	0.4623
	Meshfree [75]	0.2111	0.3852	0.3853	0.4636	0.4636

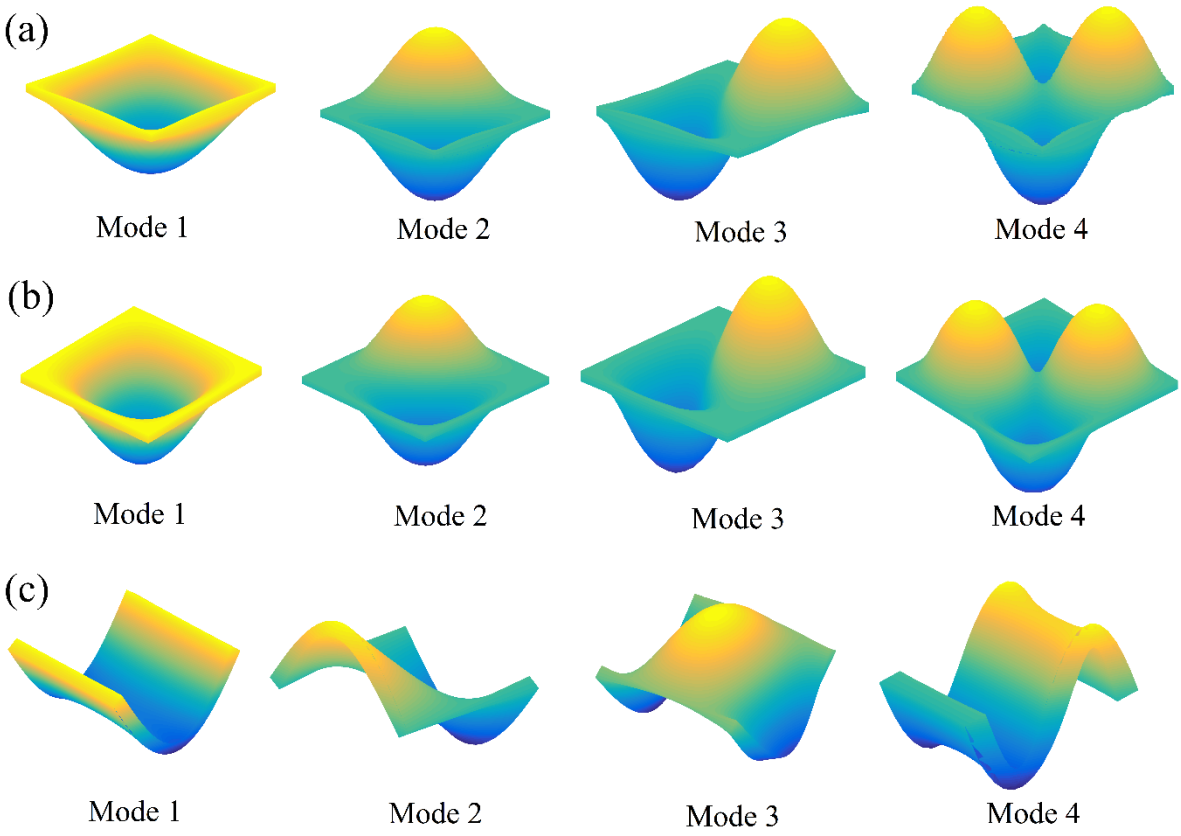

Fig. 15. The first four vibration modes of the FGM plate under various boundary conditions: (a) SSSS, (b) CCCC and (c) SFSF.

4.2.2. Circular plate

A clamped circular FGM plate is taken into account as shown in Fig. 10. IGA elements are used to cover a narrow band on the curved circumferential edge as shown in Fig. 11. In the first example, the distribution of material properties for an Al/Al_2O_3 plate is assumed to be exponential variation given in Eq. (29) in the thickness direction. The dimensionless fundamental frequency is obtained by $\overline{\omega} = \omega h\sqrt{\rho_c/C_{11}}$ where $C_{11} = E_c(1\text{-}\nu_c)/(1+\nu_c)/(1\text{-}2\nu_c)$. The dimensionless fundamental frequency for the circular FGM plate with R = 0.5 and various ratios h/R and power indices n is given in Table 7. Present results are in good agreement with the solutions acquired by the semi-analytical theory [15] and 3D Chebyshev–Ritz method [66]. The other example considers an Al/Al_2O_3 plate with various ratios h/R and

power index n = 1. The variation of the material properties in the thickness direction is based on Eqs. (49) and (50). The first five dimensionless frequencies $\bar{\omega} = 100\omega h\sqrt{\rho_c/E_c}$ of the clamped FGM plate are provided in Table 8. We can observe that the frequencies agree well with those obtained by HSDT using IGA [71], FEM [71]and uncoupled model (UM) [76]. In addition, the first six mode shapes of the circular FGM plate under clamped boundary condition are plotted in Fig. 16.

Table 7. Comparison of dimensionless fundamental frequency for the clamped Al/Al_2O_3 plate with various thickness-to-radius ratios h/R and power indices n.

h/R	Method	Power index n					
		0	**1**	**2**	**3**	**4**	**5**
0.1	Present	0.0263	0.0257	0.024	0.0217	0.0193	0.0169
	Analytical [15]	0.026	0.025	0.024	0.021	0.019	0.017
	Chebyshev-Ritz [66]	0.026	0.025	0.024	0.021	0.019	0.017
0.2	Present	0.0976	0.0955	0.0897	0.0817	0.0728	0.0643
	Analytical [15]	0.098	0.096	0.09	0.082	0.073	0.064
	Chebyshev-Ritz [66]	0.097	0.095	0.089	0.081	0.072	0.064
0.4	Present	0.3178	0.312	0.2963	0.2740	0.2490	0.2242
	Analytical [15]	0.319	0.313	0.298	0.275	0.250	0.225
	Chebyshev-Ritz [66]	0.317	0.311	0.296	0.273	0.249	0.224
0.5	Present	0.4446	0.4372	0.4172	0.3887	0.3565	0.3241
	Analytical [15]	0.446	0.439	0.419	0.39	0.358	0.326
	Chebyshev-Ritz [66]	0.444	0.436	0.416	0.388	0.356	0.324

Table 8. Comparison of first five dimensionless frequencies for the clamped Al/Al_2O_3 plate with various thickness-to-radius ratios h/R.

h/R	Method	Mode number				
		1	2	3	4	5
0.001	Present	0.0245	0.0510	0.0830	0.0955	0.1228
	HSDT [71]	0.0236	0.0492	0.0807	0.0924	0.1191
	UM [76]	0.0257	0.0535	0.0877	0.1000	0.1283
	FEM [71]	0.0234	0.0486	0.0798	0.0909	0.1167
0.1	Present	2.3160	4.7189	7.5590	8.5760	10.7900
	HSDT [71]	2.3076	4.7005	7.5318	8.5380	10.7483
	UM [76]	2.5038	5.0831	8.1156	9.1931	11.5376
	FEM [71]	2.2888	4.6661	7.4808	8.4829	10.6776
0.2	Present	8.7159	16.9268	25.9490	29.1225	34.1881
	HSDT [71]	8.6787	16.8595	25.8479	29.0092	34.1893
	UM [76]	9.3162	17.9164	27.248	30.4998	-
	FEM [71]	8.6403	16.789	25.7661	28.9152	34.1893

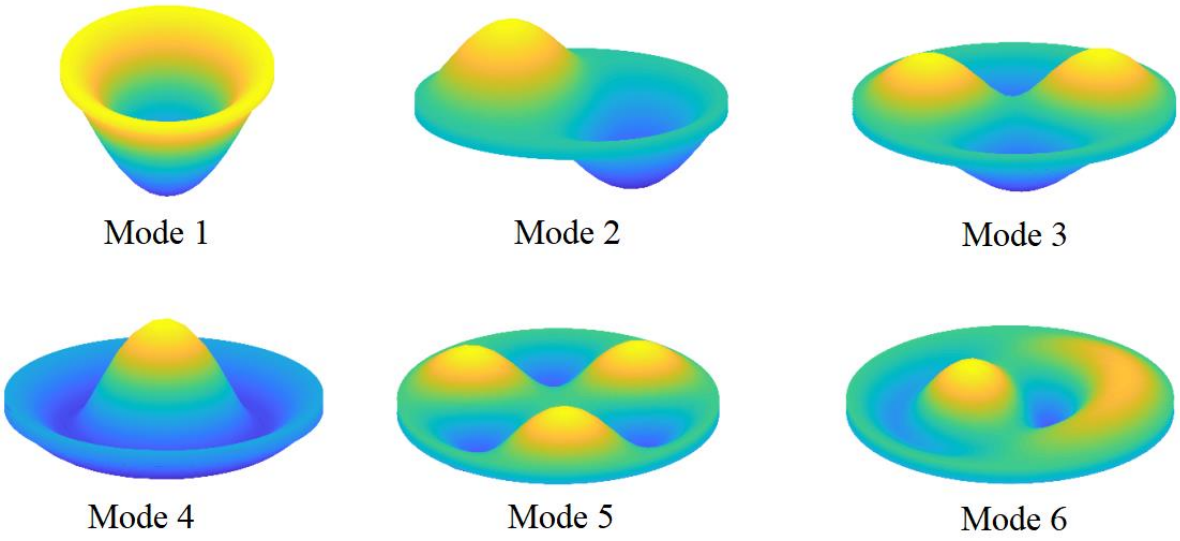

Fig. 16. The first six shape modes of the Al/Al_2O_3 plate under clamped boundary condition with $n = 1$ and $R/h = 10$.

Figs. 17 (a) and (b) give the dimensionless frequency versus the side-to-thickness ratio a/h for the rectangular plate and the radius-to-thickness ratio R/h for the circular plate,

respectively. The ingredients of the Al/Al_2O_3 plates are defined according to Eqs. (49) and (50). It is observed that the frequency reduces as the volume fraction of the metal component increases. The dimensionless fundamental frequency declines rapidly with the ratio a/h or R/h varying from 2 to 10. As a/h or R/h is between 20 and 100, the influence of two ratios on the natural frequency is small.

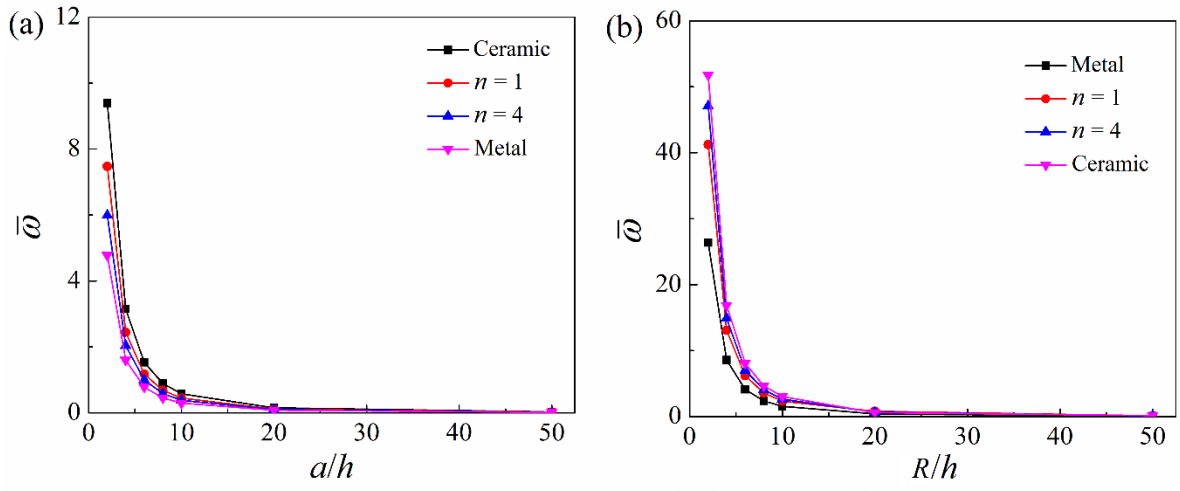

Fig. 17. Dimensionless fundamental frequency of (a) rectangular plate via the ratio a/h and (b) circular plate via the ratio R/h with various power indices n.

4.2.3. Cylindrical shell

A cylindrical shell model with graded ceramic and metal materials is shown in Fig. 18. At the mid-surface, the radius, arc length and chord length of the curvature are defined as R_m, L_R and L_x, respectively. The thickness and axial lengths are h and L_z, respectively. Material properties are assumed to vary continuously from the ceramic of outer curve to the metal of inner curve according to the rule of mixture law in Eqs. (27) and (28). The cylindrical shell is discretized by meshfree nodes and IGA elements as shown in Fig. 11. The outer and inner curves are represented by IGA elements to describe the exact curved geometry and meshfree nodes are filled into the inside domain.

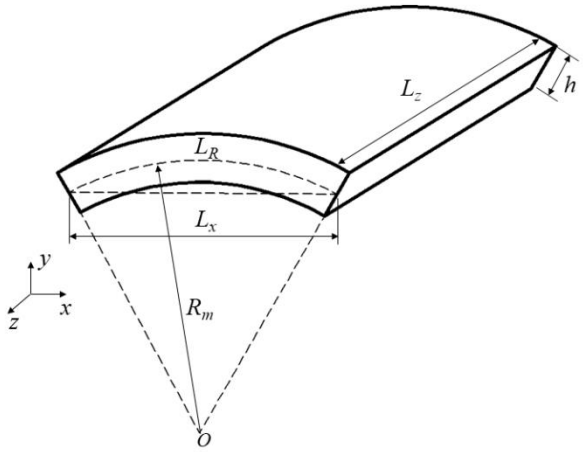

Fig. 18. Model of the FGM cylindrical shell.

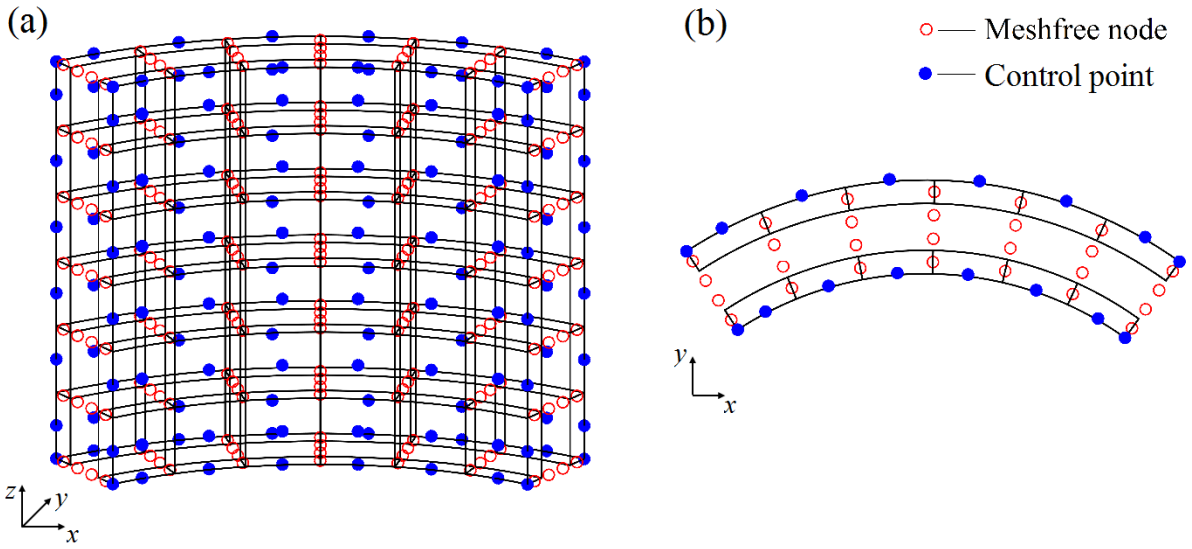

Fig. 19. Distribution of the control points and meshfree nodes for the FGM cylindrical shell: (a) 3D mesh and (b) *x*-*y* plane.

In this example, the frequency parameters $\bar{\omega} = \omega L_x\sqrt{\rho/E}$ for the isotropic cylindrical shell subjected to SSSS and CCCC boundary conditions are obtained in Table 9. We can see that a good agreement with the reported results computed by the 3D continuum and discrete approaches [16] is achieved by the present solution. To further validate our approach, the present frequency is compared with that obtained by analytical [10] and exact [12] methods in Table 10. In this case, the dimensionless frequency is normalized by $\bar{\omega} = \omega h\sqrt{\rho_c/E_c}$. The

present results demonstrate a close agreement with the results from other methods. The dimensionless fundamental frequency for the curved Al/Al_2O_3 plate with various ratios R_m/L_x and power indices n under the SSSS and CCCC boundary conditions is listed in Table 11. The first five frequencies of the curved Al/Al_2O_3 plate is given in Table 12 with various ratios L_x/h and power indices n. Furthermore, the first six mode shapes of the FGM cylindrical shell under CCCC and SSSS boundary conditions are shown in Fig. 20.

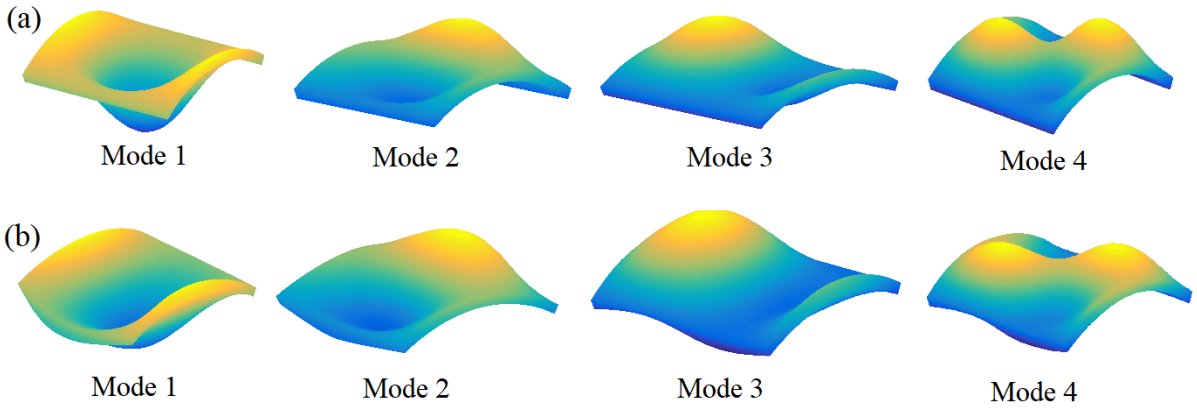

Fig. 20. The first six mode shapes of the FGM cylindrical shell under (a) CCCC and (b) SSSS boundary conditions.

Table 9. Comparison of the first five dimensionless frequencies for the isotropic cylindrical shell subjected to different boundary conditions (L_R/R_m = 0.5).

Boundary condition	L_R/h	Method	Mode number				
			1	2	3	4	5
SSSS	2	Present	1.8349	1.9278	1.9483	2.7626	3.1096
		3D solution [16]	1.8361	1.9278	1.9483	2.7626	3.1210
	5	Present	1.0576	1.9283	1.9483	2.2824	2.3415
		3D solution [16]	1.0555	1.9283	1.9483	2.2791	2.3385
CCCC	2	Present	1.6773	2.7996	2.8804	3.7415	3.7513
		3D solution [16]	1.6705	2.7905	2.8715	3.737	3.7466
	5	Present	2.3482	3.5062	3.6626	3.7526	3.7923
		3D solution [16]	2.3438	3.4994	3.6541	3.7476	3.7862

Table 10. Comparison of the dimensionless fundamental frequency for the Al/Al_2O_3 cylindrical shell under the simply supported boundary condition ($L_R = L_z$).

L_R/h	L_R/R_m	Method	Power index n					
			Ceramic	0.5	1	4	10	Metal
2	**0.5**	Present	0.9244	0.8012	0.7249	0.5784	0.5294	0.4704
		Analytical [10]	0.9187	0.8013	0.7260	0.5797	0.5245	0.4770
	1	Present	0.8854	0.7663	0.6932	0.5526	0.5059	0.4505
		Analytical [10]	0.8675	0.7578	0.687	0.5475	0.494	0.4496
5	**0.5**	Present	0.2133	0.1822	0.1643	0.1379	0.1300	0.1089
		Analytical [10]	0.2113	0.1814	0.1639	0.1413	0.1271	0.1109
		Exact [12]	0.2129	0.1817	0.1638	0.1374	0.1296	-
	1	Present	0.2158	0.1851	0.1676	0.1395	0.1302	0.1100
		Analytical [10]	0.2164	0.1852	0.1676	0.1394	0.1286	0.1133
		Exact [12]	0.2155	0.1848	0.1671	0.1392	0.1300	-

Table 11. Dimensionless fundamental frequency for the curved Al/Al_2O_3 plate with various ratios R_m/L_x and indices n under SSSS and CCCC boundary conditions ($L_x = L_z = 1$).

Boundary condition	n	R_m/L_x				
		0.5	1	2	5	10
SSSS	Ceramic	0.0957	0.0715	0.0619	0.0587	0.0582
	0.5	0.0853	0.0621	0.053	0.0499	0.0495
	1	0.0789	0.0567	0.0479	0.0450	0.0446
	4	0.0644	0.0473	0.0408	0.0387	0.0384
	10	0.0575	0.0437	0.0386	0.0369	0.0366
	Metal	0.0487	0.0366	0.0317	0.0300	0.0297
CCCC	Ceramic	0.1852	0.1320	0.1091	0.1017	0.1005
	0.5	0.1592	0.1146	0.0940	0.0872	0.0862
	1	0.1441	0.1045	0.0853	0.0789	0.0779
	4	0.1191	0.0864	0.0716	0.0667	0.066
	10	0.1105	0.0795	0.0670	0.0629	0.0623
	Metal	0.0949	0.0674	0.0559	0.0521	0.0516

Table 12. The first five frequencies of the curved Al/Al_2O_3 plate with various ratios L_x/h and power indices n ($L_x = L_z$, $L_x/R_m = 1$).

L_x/h	n	Mode number				
		1	**2**	**3**	**4**	**5**
2	Ceramic	0.8854	0.9742	0.9742	1.4169	1.6782
	1	0.6932	0.7889	0.8503	1.1794	1.3137
	4	0.5526	0.6303	0.6962	0.9414	1.0203
	10	0.5059	0.5633	0.6089	0.8419	0.9246
	Metal	0.4505	0.4954	0.4955	0.7207	0.8540
5	Ceramic	0.2158	0.3897	0.3902	0.4523	0.4796
	1	0.1675	0.3197	0.3316	0.3462	0.3746
	4	0.1395	0.2569	0.2706	0.2836	0.3068
	10	0.1302	0.2276	0.2370	0.2652	0.2844
	Metal	0.1100	0.1982	0.1984	0.2306	0.2445
10	Ceramic	0.0715	0.1353	0.1564	0.1948	0.1949
	1	0.0567	0.1032	0.1223	0.1609	0.1640
	4	0.0473	0.0875	0.1025	0.1296	0.1333
	10	0.0437	0.0833	0.0958	0.1145	0.1170
	Metal	0.0366	0.0694	0.0801	0.0991	0.0991
20	Ceramic	0.0278	0.0375	0.0539	0.0633	0.0742
	1	0.0227	0.0288	0.0433	0.0494	0.0562
	4	0.0186	0.0249	0.0361	0.0425	0.0484
	10	0.0168	0.0238	0.0332	0.0403	0.0463
	Metal	0.0143	0.0196	0.0278	0.0336	0.0384

Fig. 15 illustrate the effects of material composition, the side-to-thickness ratio and the curvature of the cylindrical shell on the natural frequency. It can be observed that a larger volume fraction of the metal ingredient can lead to the decrease of the dimensionless fundamental frequency. As the shell becomes thinner, the dimensionless fundamental frequency decreases. With increasing the ratio L_x/h, the influence of the thickness on the natural frequency decreases. To analyze the influence of the shell curvature on the frequency,

the chord length L_x and axial length L_z are fixed to be a constant. From Fig. 15 (b), it is observed that the dimensionless fundamental frequency reduces as the radius R_m increases, which means that the reduction of the curvature results in the decrease of the dimensionless fundamental frequency.

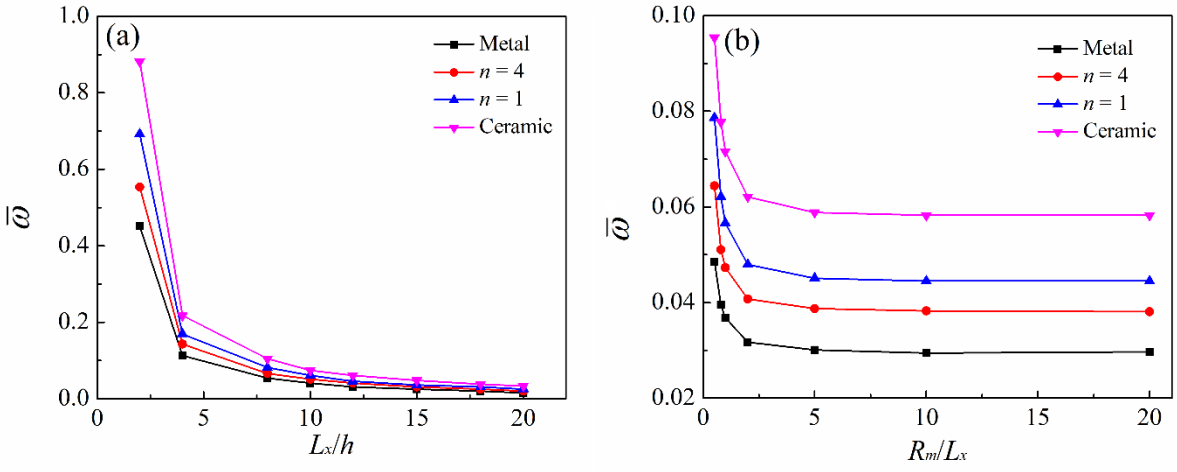

Fig. 21. Variation of the dimensionless fundamental frequency for the Al/Al_2O_3 cylindrical shell via (a) ratio L_x/h and (b) ratio R_m/L_x with various power indices n.

4.3. Buckling analyses of FGM plates and shells

The coupling approach is used to investigate the buckling behavior of the circular plate and cylindrical shell in this section. The thickness of the plate and the curvature of the cylindrical shell are analyzed.

4.3.1. Circular plate

The circular plate model is clamped and subjected to the axial uniform compression around the curved circumference, as shown in Fig. 10. The Al/ZrO_2-3 properties are given in Table 1 and material compositions are distributed in the thickness direction according to the rule of mixture law in Eqs. (49) and (50). The convergence test of the buckling load is shown in Fig. 22 with the power indices n = 2 and 10. The discretization of the circular plate is

shown in Fig. 11. We can see that results can converge to the reported solutions [77] as 5724 DOFs (24 × 24 × 3 meshfree nodes and 36 × 5 control points) are implemented. The variation of the dimensionless critical buckling load $\bar{\lambda} = \lambda R/D_m$ where $D_m = E_m h^3/(12(1-\nu_m^2))$ with different power indices n and radius-to-thickness ratios R/h is tabulated in Table 13. To verify the validation of the coupling approach for the buckling analysis, the present results are compared with those acquired from the TSDT [78], unstrained TDST (UTSDT) [77] and HSDT using IGA [70] and a good agreement is obtained. The variation of the buckling load for the Al/ZrO_2-3 circular plate with the radius-to-thickness ratio R/h is shown in Fig. 23. It is observed that the dimensionless buckling load rises as the ceramic volume fraction increases. As the plate becomes thinner, the dimensionless buckling load increases quickly ($R/h < 10$) and changes hardly ($R/h > 20$).

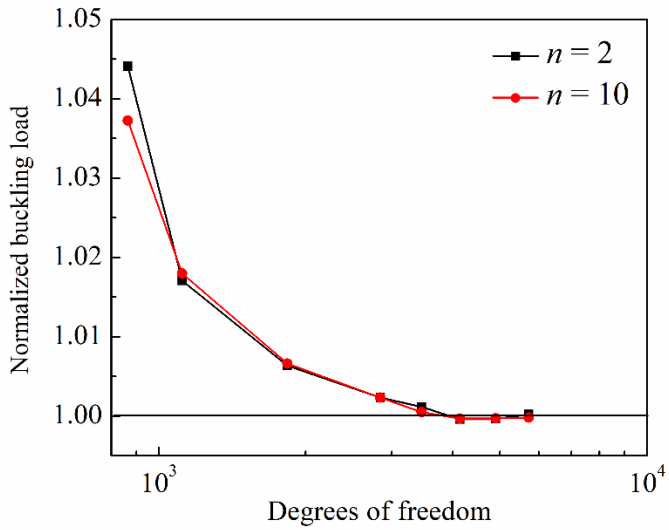

Fig. 22. Convergence test of the normalized critical buckling load for the clamped Al/ZrO_2-3 circular plate at $h/R_m = 10$ [77].

Table 13. Comparison of the dimensionless critical buckling load for the Al/ZrO_2-3 circular plate under the clamped boundary condition with R = 0.5.

h/R_m	Method	Power index n				
		0	**0.5**	**2**	**5**	**10**
0.1	Present	14.0836	19.3927	23.0797	25.4322	27.116
	TSDT [78]	14.089	19.423	23.057	25.411	27.111
	UTSDT [77]	14.089	19.413	23.075	25.422	27.131
	IGA [70]	14.1089	19.4391	23.1062	25.4743	27.1684
0.2	Present	12.4752	17.1249	20.5414	22.6912	24.1759
	TSDT [78]	12.571	17.340	20.742	22.876	24.353
	UTSDT [77]	12.575	17.310	20.8319	22.969	24.422
	IGA [70]	12.5914	17.3327	20.8319	22.9918	24.4542
0.25	Present	11.4847	15.7847	19.1774	21.1906	22.4019
	TSDT [78]	11.631	16.048	19.290	21.282	22.627
	UTSDT [77]	11.639	16.012	19.378	21.412	22.725
	IGA [70]	11.6540	16.0120	19.4033	21.4407	22.7536
0.3	Present	10.6424	14.8113	17.7234	19.6436	21.0663
	TSDT [78]	10.657	14.711	17.770	19.611	20.823
	UTSDT [77]	10.670	14.672	17.882	19.780	20.948
	IGA [70]	10.6842	14.6910	17.9060	19.8042	20.9750

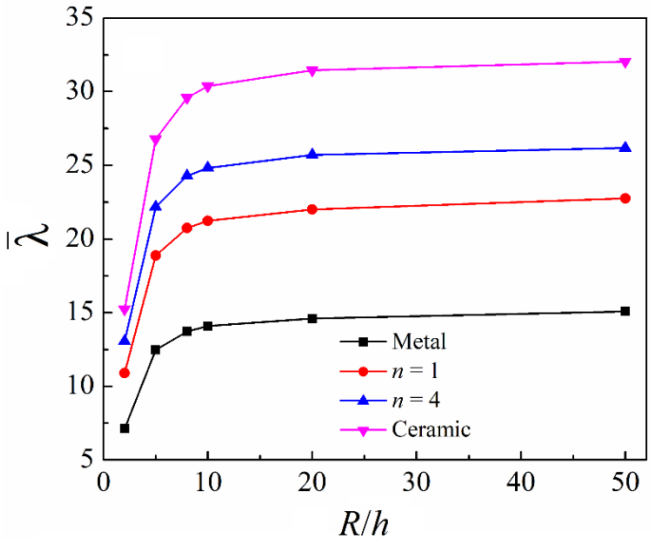

Fig. 23. Dimensionless buckling load of Al/ZrO_2-3 circular plate via the radius-to-thickness ratio R/h with various power indices n.

4.3.2. Cylindrical shell

An FGM cylindrical shell as shown in Fig. 18 under a uniform axial compression along its curved edges is first considered to study the buckling response. The rule of mixture law in Eqs. (27) and (28) is employed to describe the material distribution. The buckling load is normalized using the formula $\bar{\lambda} = \lambda R_m/(E_m h^2)$. From the convergence test in Table 14, a mesh with 18 × 18 × 3 meshfree nodes and 19 × 19 × 2 control points is used for the following examples. The dimensional buckling load for the Al/ZrO_2-3 cylindrical shell under the SSSS boundary condition with various power indices n and curvatures of the cylindrical shell is listed in Table 15. In the second case, the buckling analysis for a semi-circular cylindrical shell subjected to the axial load f_0 as shown in Fig. 24 is conducted. The first five dimensionless critical buckling loads for the semi-circular Al/ZrO_2-3 cylindrical shell with two clamped straight edges and two free curved edges are given in Table 16. Furthermore, the fundamental buckling mode shape of Al/ZrO_2-3 semi-circular cylindrical shell subjected to an axial compression under various boundary conditions are demonstrated in Fig. 25. The CSCS boundary condition indicates that the two straight edges are clamped, while the other two edges are simply supported.

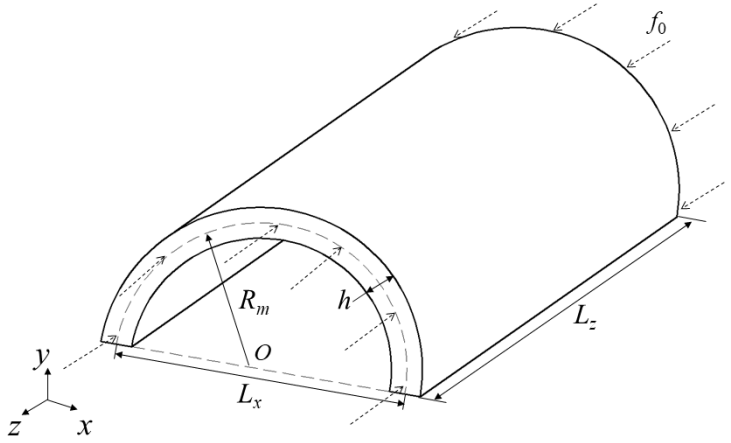

Fig. 24. Model of the FGM semi-circular cylindrical shell.

Table 14. Convergence of the dimensionless critical buckling load for the Al/ZrO_2-3 cylindrical shell under the simply supported boundary condition (L_z = 0.2, R_m = 1, L_R/R_m = 0.2 and n = 0.5).

L_z/h	Present					Ref. [79]
	8 × 8 × 3	10 × 10 × 3	12 × 12 × 3	16 × 16 × 3	18 × 18 × 3	
10	3.0336	2.9684	2.9661	2.9594	2.9533	2.9718
20	1.8130	1.7309	1.7013	1.6829	1.6801	1.6831
30	1.6555	1.4196	1.3431	1.2958	1.2876	1.2817
40	1.9676	1.4141	1.2533	1.1580	1.1418	1.1127

Table 15. Dimensionless critical buckling load for the Al/ZrO_2-3 cylindrical shell under the simply supported boundary condition ($L_x = L_z$ = 1).

n	R_m/L_x				
	0.5	**1**	**2**	**5**	**10**
Ceramic	1.7146	1.1104	0.8286	0.75402	0.74351
0.5	1.3832	0.8885	0.65335	0.59188	0.58353
1	1.2336	0.7914	0.5824	0.52808	0.5208
4	0.9982	0.6475	0.4917	0.4514	0.44604
10	0.9062	0.5908	0.45265	0.4166	0.41171
Metal	0.7964	0.5158	0.3853	0.35024	0.34529

Table 16. The first five dimensionless critical buckling load for the Al/ZrO_2-3 semi-circular cylindrical shell with various power indices ($L_z = 2L_x$ and $L_R = \pi R$).

Mode number	**Power index n**					
	Ceramic	**0.5**	1	**4**	**10**	**Metal**
1	0.5275	0.4182	0.3729	0.3105	0.2850	0.2456
2	0.5813	0.4644	0.4136	0.3387	0.3093	0.2695
3	0.6116	0.4891	0.4356	0.3567	0.3256	0.2836
4	0.6210	0.4961	0.4419	0.3623	0.3310	0.2880
5	0.6516	0.5196	0.4627	0.3804	0.348	0.3024

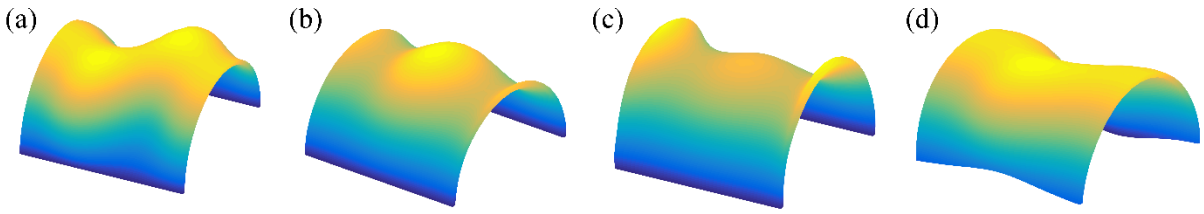

Fig. 25. Fundamental buckling mode shape of the Al/ZrO_2-3 semi-circular cylindrical shell under (a) CCCC, (b) CSCS, (c) CFCF and (d) SSSS boundary conditions ($L_z = 2L_x$, $L_R = \pi R$ and $n = 1$).

The effects of the side-to-side ratio L_z/L_x and the radius-to-side ratio R_m/L_x for the FGM cylindrical shell on the buckling load are illustrated in Fig. 26. It is noted that the dimensionless buckling load decreases with the raising of the power index n, and the shell stiffness becomes low with the increasing volume fraction of the metal ingredient. From Fig. 26 (a), we can see that the dimensionless buckling load declines as the side-to-side ratio L_z/L_x increases. As the ratio R_m/L_x increases, which leads to a flatter cylindrical shell, the dimensionless buckling load decreases. A sharp decrease of the buckling load occurs as $R_m/L_x < 5$ and the dimensionless buckling load gradually approaches a constant value as the shell becomes flatter.

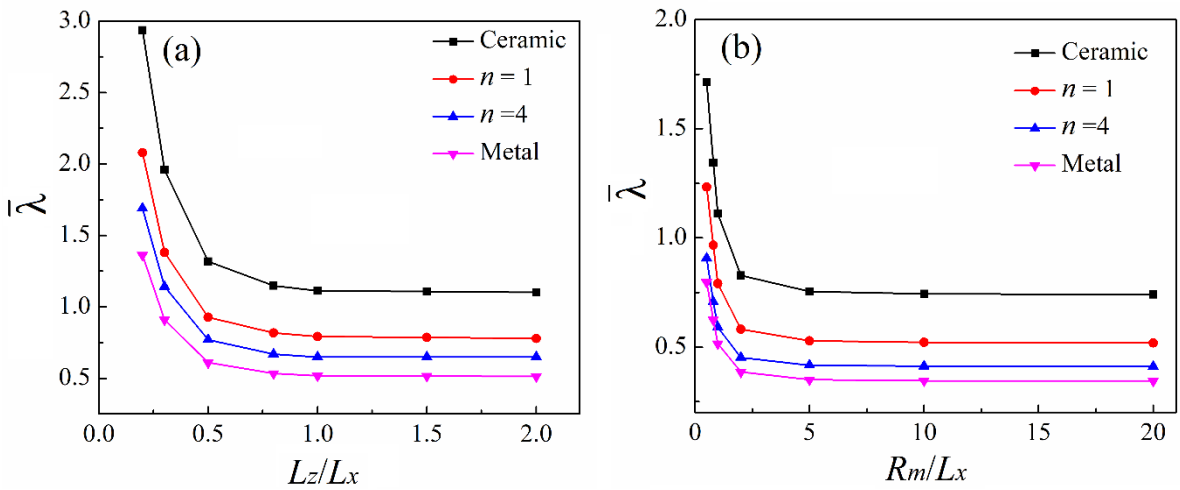

Fig. 26. Dimensionless buckling load of the Al/ZrO_2-3 cylindrical shell via the side-to-side ratio L_z/L_x and the radius-to-side ratio R_m/L_x with various power indices n.

5. Conclusions

This paper develops a 3D IGA-meshfree coupling approach to analyze FGM plates and shells. By employing the higher-order consistency condition to couple the IGA and RKPM in the physical domain, the approach can achieve higher-order smoothness of basis functions, and reduce the difficulty of creating the 3D geometry, which results from the global volumetric parameterization of IGA. In the coupling approach, IGA elements and meshfree nodes are used to represent the problem domain boundary and discretize the interior domain, respectively, incorporating advantages of the exact representation of the geometry for IGA and flexible nodes distribution for the meshfree method. Based on the coupling approach, the 3D analysis formulations for the static, dynamic and buckling behaviours of FGM plates and shells are established. From the numerical examples, the present results are in a good agreement with other analytical or numerical solutions, showing strong validation for the coupling approach.

From the static analysis for FGM plates, it can be found that the dimensionless deflection decreases with the increase of the plate thickness and the metal volume fraction. The dynamic analysis of FGM plates and cylindrical shells reveals that the increase of the thickness and the metal ingredient leads to the decrease of the dimensionless fundamental frequency. For the cylindrical shell, the dimensionless frequency reduces as the curvature of the cylinder shell decreases. From the buckling analysis, the dimensionless buckling load of the circular plate and cylindrical shell increases with the rising volume fraction of ceramic, while decreasing the curvature of the cylindrical shell results in the decline of the dimensionless buckling load.

Acknowledgements

The authors acknowledge the financial supports from the Ministry of Education, Singapore (Academic Research Fund TIER 1-RG174/15), Singapore Maritime Institute (Grant No: SMI-2014-MA11) and the National Research Foundation Medium Sized Centre, Singapore through the Marine and Offshore Program.

References

[1] Timoshenko SP, Woinowsky-Krieger S. Theory of plates and shells. New York: McGraw-hill, 1959.

[2] Reissner E. The effect of transverse shear deformation on the bending of elastic plates. Journal of applied mechanics. 1945;12:69-77.

[3] Mindlin R. Influence of rotatory inertia and shear on flexural motions of isotropic, elastic plates. Journal of applied mechanics. 1951;18:31.

[4] Reddy JN. A simple higher-order theory for laminated composite plates. Journal of applied mechanics. 1984;51:745-52.

[5] Pradyumna S, Bandyopadhyay JN. Free vibration analysis of functionally graded curved panels using a higher-order finite element formulation. Journal of Sound and Vibration. 2008;318:176-92.

[6] Tornabene F. Free vibration analysis of functionally graded conical, cylindrical shell and annular plate structures with a four-parameter power-law distribution. Computer Methods in Applied Mechanics and Engineering. 2009;198:2911-35.

[7] Tornabene F, Viola E, Fantuzzi N. General higher-order equivalent single layer theory for free vibrations of doubly-curved laminated composite shells and panels. Composite Structures. 2013;104:94-117.

[8] Matsunaga H. Free vibration and stability of functionally graded shallow shells according to a 2D higher-order deformation theory. Composite Structures. 2008;84:132-46.

[9] Su Z, Jin G, Ye T. Three-dimensional vibration analysis of thick functionally graded conical, cylindrical shell and annular plate structures with arbitrary elastic restraints. Composite Structures. 2014;118:432-47.

[10] Zahedinejad P, Malekzadeh P, Farid M, Karami G. A semi-analytical three-dimensional free vibration analysis of functionally graded curved panels. International Journal of Pressure Vessels and Piping. 2010;87:470-80.

[11] Nguyen KD, Nguyen-Xuan H. An isogeometric finite element approach for three-dimensional static and dynamic analysis of functionally graded material plate structures. Composite Structures. 2015;132:423-39.

[12] Brischetto S, Tornabene F, Fantuzzi N, Viola E. 3D exact and 2D generalized differential quadrature models for free vibration analysis of functionally graded plates and cylinders. Meccanica. 2016;51:2059-98.

[13] Asemi K, Shariyat M. Highly accurate nonlinear three-dimensional finite element elasticity approach for biaxial buckling of rectangular anisotropic FGM plates with general orthotropy directions. Composite Structures. 2013;106:235-49.

[14] Giunta G, Belouettar S, Ferreira AJM. A static analysis of three-dimensional functionally graded beams by hierarchical modelling and a collocation meshless solution method. Acta Mechanica. 2015;227:969-91.

[15] Nie GJ, Zhong Z. Semi-analytical solution for three-dimensional vibration of functionally graded circular plates. Computer Methods in Applied Mechanics and Engineering. 2007;196:4901-10.

[16] Liew K, Bergman L, Ng T, Lam K. Three-dimensional vibration of cylindrical shell panels–solution by continuum and discrete approaches. Computational Mechanics. 2000;26:208-21.

[17] Hosseini-Hashemi S, Fadaee M, Atashipour SR. A new exact analytical approach for free vibration of Reissner–Mindlin functionally graded rectangular plates. International Journal of Mechanical Sciences. 2011;53:11-22.

[18] Vel SS, Batra RC. Exact Solution for Thermoelastic Deformations of Functionally Graded Thick Rectangular Plates. AIAA Journal. 2002;40:1421-33.

[19] Farid M, Zahedinejad P, Malekzadeh P. Three-dimensional temperature dependent free vibration analysis of functionally graded material curved panels resting on two-parameter elastic foundation using a hybrid semi-analytic, differential quadrature method. Materials & Design. 2010;31:2-13.

[20] Kadoli R, Ganesan N. Buckling and free vibration analysis of functionally graded cylindrical shells subjected to a temperature-specified boundary condition. Journal of Sound and Vibration. 2006;289:450-80.

[21] Bhangale RK, Ganesan N. Free vibration studies of simply supported non-homogeneous functionally graded magneto-electro-elastic finite cylindrical shells. Journal of Sound and Vibration. 2005;288:412-22.

[22] Afsar AM, Go J. Finite element analysis of thermoelastic field in a rotating FGM circular disk. Applied Mathematical Modelling. 2010;34:3309-20.

[23] Reddy J. Analysis of functionally graded plates. International Journal for Numerical Methods in Engineering. 2000;47:663-84.

[24] Zhu P, Lei ZX, Liew KM. Static and free vibration analyses of carbon nanotube-reinforced composite plates using finite element method with first order shear deformation plate theory. Composite Structures. 2012;94:1450-60.

[25] Liew KM, Zhao X, Ferreira AJM. A review of meshless methods for laminated and functionally graded plates and shells. Composite Structures. 2011;93:2031-41.

[26] Gingold RA, Monaghan JJ. Smoothed particle hydrodynamics: theory and application to non-spherical stars. Monthly notices of the royal astronomical society. 1977;181:375-89.

[27] Nayroles B, Touzot G, Villon P. Generalizing the finite element method: diffuse approximation and diffuse elements. Computational Mechanics. 1992;10:307-18.

[28] Belytschko T, Lu YY, Gu L. Element‐free Galerkin methods. International Journal for Numerical Methods in Engineering. 1994;37:229-56.

[29] Atluri SN, Zhu T. A new meshless local Petrov-Galerkin (MLPG) approach in computational mechanics. Computational Mechanics. 1998;22:117-27.

[30] Liu WK, Jun S, Zhang YF. Reproducing kernel particle methods. International journal for numerical methods in fluids. 1995;20:1081-106.

[31] Chen J-S, Pan C, Wu C-T, Liu WK. Reproducing kernel particle methods for large deformation analysis of non-linear structures. Computer Methods in Applied Mechanics and Engineering. 1996;139:195-227.

[32] Liu WK, Jun S, Li S, Adee J, Belytschko T. Reproducing kernel particle methods for structural dynamics. International Journal for Numerical Methods in Engineering. 1995;38:1655-79.

[33] Ferreira AJM, Batra RC, Roque CMC, Qian LF, Martins PALS. Static analysis of functionally graded plates using third-order shear deformation theory and a meshless method. Composite Structures. 2005;69:449-57.

[34] Rezaei Mojdehi A, Darvizeh A, Basti A, Rajabi H. Three dimensional static and dynamic analysis of thick functionally graded plates by the meshless local Petrov–Galerkin (MLPG) method. Engineering Analysis with Boundary Elements. 2011;35:1168-80.

[35] Dai KY, Liu GR, Lim KM, Han X, Du SY. A meshfree radial point interpolation method for analysis of functionally graded material (FGM) plates. Computational Mechanics. 2004;34.

[36] Zhao X, Liew KM. Free vibration analysis of functionally graded conical shell panels by a meshless method. Composite Structures. 2011;93:649-64.

[37] Neves AMA, Ferreira AJM, Carrera E, Cinefra M, Roque CMC, Jorge RMN, et al. Static, free vibration and buckling analysis of isotropic and sandwich functionally graded plates using a quasi-3D higher-order shear deformation theory and a meshless technique. Composites Part B: Engineering. 2013;44:657-74.

[38] Dai KY, Liu GR, Han X, Lim KM. Thermomechanical analysis of functionally graded material (FGM) plates using element-free Galerkin method. Computers & Structures. 2005;83:1487-502.

[39] Phan-Dao H-H, Thai CH, Lee J, Nguyen-Xuan H. Analysis of laminated composite and sandwich plate structures using generalized layerwise HSDT and improved meshfree radial point interpolation method. Aerospace Science and Technology. 2016;58:641-60.

[40] Thai CH, Do VNV, Nguyen-Xuan H. An improved Moving Kriging-based meshfree method for static, dynamic and buckling analyses of functionally graded isotropic and sandwich plates. Engineering Analysis with Boundary Elements. 2016;64:122-36.

[41] Thai CH, Ferreira AJM, Nguyen-Xuan H. Naturally stabilized nodal integration meshfree formulations for analysis of laminated composite and sandwich plates. Composite Structures. 2017;178:260-76.

[42] Thai CH, Nguyen TN, Rabczuk T, Nguyen-Xuan H. An improved moving Kriging meshfree method for plate analysis using a refined plate theory. Computers & Structures. 2016;176:34-49.

[43] Li W, Nguyen-Thanh N, Zhou K. Geometrically nonlinear analysis of thin-shell structures based on an isogeometric-meshfree coupling approach. Computer Methods in Applied Mechanics and Engineering. 2018.

[44] Nguyen-Thanh N, Li W, Zhou K. Static and free-vibration analyses of cracks in thin-shell structures based on an isogeometric-meshfree coupling approach. Computational Mechanics. 2018:1-23.

[45] Nguyen-Thanh N, Huang J, Zhou K. An isogeometric-meshfree coupling approach for analysis of cracks. International Journal for Numerical Methods in Engineering. 2018;113:1630-51.

[46] Hughes TJR, Cottrell JA, Bazilevs Y. Isogeometric analysis: CAD, finite elements, NURBS, exact geometry and mesh refinement. Computer Methods in Applied Mechanics and Engineering. 2005;194:4135-95.

[47] Valizadeh N, Natarajan S, Gonzalez-Estrada OA, Rabczuk T, Bui TQ, Bordas SPA. NURBS-based finite element analysis of functionally graded plates: Static bending, vibration, buckling and flutter. Composite Structures. 2013;99:309-26.

[48] Nguyen-Thanh N, Valizadeh N, Nguyen MN, Nguyen-Xuan H, Zhuang X, Areias P, et al. An extended isogeometric thin shell analysis based on Kirchhoff–Love theory. Computer Methods in Applied Mechanics and Engineering. 2015;284:265-91.

[49] Nguyen-Thanh N, Zhou K, Zhuang X, Areias P, Nguyen-Xuan H, Bazilevs Y, et al. Isogeometric analysis of large-deformation thin shells using RHT-splines for multiple-patch coupling. Computer Methods in Applied Mechanics and Engineering. 2017;316:1157-78.

[50] Cottrell JA, Reali A, Bazilevs Y, Hughes TJR. Isogeometric analysis of structural vibrations. Computer Methods in Applied Mechanics and Engineering. 2006;195:5257-96.

[51] Anitescu C, Hossain MN, Rabczuk T. Recovery-based error estimation and adaptivity using high-order splines over hierarchical T-meshes. Computer Methods in Applied Mechanics and Engineering. 2018;328:638-62.

[52] Tan P, Nguyen-Thanh N, Zhou K. Extended isogeometric analysis based on Bézier extraction for an FGM plate by using the two-variable refined plate theory. Theoretical and Applied Fracture Mechanics. 2017;89:127-38.

[53] Ghorashi SS, Valizadeh N, Mohammadi S. Extended isogeometric analysis for simulation of stationary and propagating cracks. International Journal for Numerical Methods in Engineering. 2012;89:1069-101.

[54] Nguyen-Thanh N, Zhou K. Extended isogeometric analysis based on PHT-splines for crack propagation near inclusions. International Journal for Numerical Methods in Engineering. 2017.

[55] Bazilevs Y, Calo VM, Zhang Y, Hughes TJR. Isogeometric Fluid–structure Interaction Analysis with Applications to Arterial Blood Flow. Computational Mechanics. 2006;38:310-22.

[56] Nguyen-Thanh N, Kiendl J, Nguyen-Xuan H, Wüchner R, Bletzinger KU, Bazilevs Y, et al. Rotation free isogeometric thin shell analysis using PHT-splines. Computer Methods in Applied Mechanics and Engineering. 2011;200:3410-24.

[57] Benson DJ, Bazilevs Y, Hsu MC, Hughes TJR. Isogeometric shell analysis: The Reissner–Mindlin shell. Computer Methods in Applied Mechanics and Engineering. 2010;199:276-89.

[58] Tran LV, Ferreira AJM, Nguyen-Xuan H. Isogeometric analysis of functionally graded plates using higher-order shear deformation theory. Composites Part B: Engineering. 2013;51:368-83.

[59] Nguyen-Xuan H, Tran LV, Thai CH, Kulasegaram S, Bordas SPA. Isogeometric analysis of functionally graded plates using a refined plate theory. Composites Part B: Engineering. 2014;64:222-34.

[60] Thai CH, Zenkour AM, Abdel Wahab M, Nguyen-Xuan H. A simple four-unknown shear and normal deformations theory for functionally graded isotropic and sandwich plates based on isogeometric analysis. Composite Structures. 2016;139:77-95.

[61] Chan C, Anitescu C, Rabczuk T. Isogeometric analysis with strong multipatch C^1-coupling. Computer Aided Geometric Design. 2018;In Press.

[62] Wang D, Zhang H. A consistently coupled isogeometric–meshfree method. Computer Methods in Applied Mechanics and Engineering. 2014;268:843-70.

[63] Rosolen A, Arroyo M. Blending isogeometric analysis and local maximum entropy meshfree approximants. Computer Methods in Applied Mechanics and Engineering. 2013;264:95-107.

[64] Valizadeh N, Bazilevs Y, Chen JS, Rabczuk T. A coupled IGA–Meshfree discretization of arbitrary order of accuracy and without global geometry parameterization. Computer Methods in Applied Mechanics and Engineering. 2015;293:20-37.

[65] Liu G-R. Mesh free methods: moving beyond the finite element method: CRC press, 2002.

[66] Dong CY. Three-dimensional free vibration analysis of functionally graded annular plates using the Chebyshev–Ritz method. Materials & Design. 2008;29:1518-25.

[67] Zhong Z, Shang ET. Three-dimensional exact analysis of a simply supported functionally gradient piezoelectric plate. International Journal of Solids and Structures. 2003;40:5335-52.

[68] Reddy JN. Mechanics of laminated composite plates and shells: theory and analysis: CRC press, 2004.

[69] Fernández-Méndez S, Huerta A. Imposing essential boundary conditions in mesh-free methods. Computer Methods in Applied Mechanics and Engineering. 2004;193:1257-75.

[70] Tran LV, Ferreira A, Nguyen-Xuan H. Isogeometric analysis of functionally graded plates using higher-order shear deformation theory. Composites Part B: Engineering. 2013;51:368-83.

[71] Gilhooley D, Batra R, Xiao J, McCarthy M, Gillespie J. Analysis of thick functionally graded plates by using higher-order shear and normal deformable plate theory and MLPG method with radial basis functions. Composite Structures. 2007;80:539-52.

[72] Reddy J, Wang C, Kitipornchai S. Axisymmetric bending of functionally graded circular and annular plates. European Journal of Mechanics-A/Solids. 1999;18:185-99.

[73] Ferreira A, Batra R, Roque C, Qian L, Martins P. Static analysis of functionally graded plates using third-order shear deformation theory and a meshless method. Composite Structures. 2005;69:449-57.

[74] Nguyen T-K, Sab K, Bonnet G. First-order shear deformation plate models for functionally graded materials. Composite Structures. 2008;83:25-36.

[75] Qian L, Batra R, Chen L. Static and dynamic deformations of thick functionally graded elastic plates by using higher-order shear and normal deformable plate theory and meshless local Petrov–Galerkin method. Composites Part B: Engineering. 2004;35:685-97.

[76] Ebrahimi F, Rastgoo A, Atai AA. A theoretical analysis of smart moderately thick shear deformable annular functionally graded plate. European Journal of Mechanics - A/Solids. 2009;28:962-73.

[77] Ma LS, Wang TJ. Relationships between axisymmetric bending and buckling solutions of FGM circular plates based on third-order plate theory and classical plate theory. International Journal of Solids and Structures. 2004;41:85-101.

[78] Saidi AR, Rasouli A, Sahraee S. Axisymmetric bending and buckling analysis of thick functionally graded circular plates using unconstrained third-order shear deformation plate theory. Composite Structures. 2009;89:110-9.

[79] Huan DT, Tu TM, Quoc TH. Analytical solutions for bending, buckling and vibration analysis of functionally graded cylindrical panel. Vietnam Journal of Science and Technology. 2017;55:587.